

Galaxies in X-ray selected clusters and groups in Dark Energy Survey data – II. Hierarchical Bayesian modelling of the red-sequence galaxy luminosity function

Y. Zhang¹★, C. J. Miller,^{2,3} P. Rooney,⁴ A. Bermeo,⁴ A. K. Romer,⁴ C. Vergara Cervantes,⁴ E. S. Rykoff,^{5,6} C. Hennig,^{7,8} R. Das,³ T. McKay,³ J. Song,⁹ H. Wilcox,¹⁰ D. Bacon,¹⁰ S. L. Bridle,¹¹ C. Collins,¹² C. Conselice,¹³ M. Hilton,¹⁴ B. Hoyle,¹⁵ S. Kay,¹⁶ A. R. Liddle,¹⁷ R. G. Mann,¹⁸ N. Mehrrens,¹⁹ J. Mayers,⁴ R. C. Nichol,¹⁰ M. Sahlén,²⁰ J. Stott,²¹ P. T. P. Viana,^{22,23} R. H. Wechsler,^{5,6,24} T. Abbott,²⁵ F. B. Abdalla,^{26,27} S. Allam,¹ A. Benoit-Lévy,^{26,28,29} D. Brooks,²⁶ E. Buckley-Geer,¹ D. L. Burke,^{5,6} A. Carnero Rosell,^{30,31} M. Carrasco Kind,^{32,33} J. Carretero,³⁴ F. J. Castander,³⁵ M. Crocce,³⁵ C. E. Cunha,⁵ C. B. D’Andrea,³⁶ L. N. da Costa,^{30,31} H. T. Diehl,¹ J. P. Dietrich,^{7,8} T. F. Eifler,^{37,38} B. Flaugher,¹ P. Fosalba,³⁵ J. García-Bellido,³⁹ E. Gaztanaga,³⁵ D. W. Gerdes,^{2,3} D. Gruen,^{5,6} R. A. Gruendl,^{32,33} J. Gschwend,^{30,31} G. Gutierrez,¹ K. Honscheid,^{40,41} D. J. James,⁴² T. Jeltema,⁴³ K. Kuehn,⁴⁴ N. Kuropatkin,¹ M. Lima,^{30,45} H. Lin,¹ M. A. G. Maia,^{30,31} M. March,³⁶ J. L. Marshall,¹⁹ P. Melchior,⁴⁶ F. Menanteau,^{32,33} R. Miquel,^{34,47} R. L. C. Ogando,^{30,31} A. A. Plazas,³⁸ E. Sanchez,⁴⁸ M. Schubnell,³ I. Sevilla-Noarbe,⁴⁸ M. Smith,⁴⁹ M. Soares-Santos,¹ F. Sobreira,^{30,50} E. Suchyta,⁵¹ M. E. C. Swanson,³³ G. Tarle,³ and A. R. Walker²⁵ (DES Collaboration)

Affiliations are listed at the end of the paper

Accepted 2019 June 5. Received 2019 June 5; in original form 2019 April 13

ABSTRACT

Using ~ 100 X-ray selected clusters in the Dark Energy Survey Science Verification data, we constrain the luminosity function (LF) of cluster red-sequence galaxies as a function of redshift. This is the first homogeneous optical/X-ray sample large enough to constrain the evolution of the LF simultaneously in redshift ($0.1 < z < 1.05$) and cluster mass ($13.5 \leq \log_{10}(M_{200\text{crit}}) < 15.0$). We pay particular attention to completeness issues and the detection limit of the galaxy sample. We then apply a hierarchical Bayesian model to fit the cluster galaxy LFs via a Schechter function, including its characteristic break (m^*) to a faint end power-law slope (α). Our method enables us to avoid known issues in similar analyses based on stacking or binning the clusters. We find weak and statistically insignificant ($\sim 1.9\sigma$) evolution in the faint end slope α versus redshift. We also find no dependence in α or m^* with the X-ray inferred cluster masses. However, the amplitude of the LF as a function of cluster mass is constrained to ~ 20 per cent precision. As a by-product of our algorithm, we utilize the correlation between the LF and cluster mass to provide an improved estimate of the individual cluster masses as well as the scatter in true mass given the X-ray inferred masses. This technique can be applied to a larger sample of X-ray or optically selected clusters from the Dark Energy Survey, significantly improving the sensitivity of the analysis.

Key words: galaxies: clusters: general – galaxies: evolution.

★ E-mail: ynzhang@fnal.gov

1 INTRODUCTION

Galaxy clusters are special for both cosmology and astrophysics studies. As the structures that correspond to the massive end of halo mass function, they are sensitive probes of the Λ cold dark matter cosmological model (see reviews in Allen, Evrard & Mantz 2011; Weinberg et al. 2013). As the most massive virialized structures in the Universe, they provide the sites for studying astrophysical processes in dense environments.

Galaxy clusters are known to harbour red-sequence (RS) galaxies, so named because these galaxies rest on a tight relation in the colour–magnitude space (Bower, Lucey & Ellis 1992). The phenomenon has been employed in finding clusters from optical data (e.g. Gladders & Yee 2000; Miller et al. 2005; Koester et al. 2007; Rykoff et al. 2016; Oguri et al. 2018) and developing cluster mass proxies (e.g. Rykoff et al. 2012). RS galaxies also attract attention in astrophysics studies as they exhibit little star formation activity. Their formation and evolution provide clues to how quenching of galaxy star formation occurs in the cluster environment.

It is well-established that the massive RS galaxies form at an early epoch (e.g. Mullis et al. 2005; Stanford et al. 2005; Mei et al. 2006; Eisenhardt et al. 2008; Hilton et al. 2009; Kurk et al. 2009; Papovich et al. 2010; Gobat et al. 2011; Jaffé et al. 2011; Grützbauch et al. 2012; Tanaka et al. 2013), but the formation of faint RS galaxies can be better characterized. The latter could be examined through inspecting the luminosity distribution of cluster galaxies, either with the dwarf-to-giant ratio approach (De Lucia et al. 2007), or as adopted in this paper, with a luminosity function (LF) analysis. Results from these analyses are controversial to date, and have been extensively reviewed in literature (e.g. Faber et al. 2007; Crawford, Bershady & Hoessel 2009; Boselli & Gavazzi 2014; Wen & Han 2015).

To summarize, a few studies have reported a deficit of faint RS galaxies with increasing redshift (De Lucia et al. 2007; Stott et al. 2007; Gilbank et al. 2008; Rudnick et al. 2009; Capozzi, Collins & Stott 2010; de Filippis et al. 2011; Martinet et al. 2015; Lin et al. 2017), indicating later formation of faint RS galaxies compared to the bright (and massive) ones. Yet, many other works observe little evolution in the RS luminosity distribution up to redshift 1.5 (Andreon 2008; Crawford et al. 2009; De Propriis, Phillipps & Bremer 2013; De Propriis, Bremer & Phillipps 2015, 2016; Cerulo et al. 2016; Connor et al. 2017; Sarron et al. 2018), suggesting an early formation of both faint and bright RS galaxies. Differences in these results are hard to interpret given the different methods (see the discussion in Crawford et al. 2009), sample selections and possible dependence on cluster mass (Gilbank et al. 2008; Hansen et al. 2009; Lan, Ménard & Mo 2016), dynamical states (De Propriis et al. 2013; Wen & Han 2015), and whether or not the clusters are fossils (Zarattini et al. 2015). Carrying out more detailed analyses, especially in the 0.5–1.0 redshift range, may help resolve the differences.

The luminosity distribution of cluster galaxies has also been modelled to connect galaxies with the underlying dark matter distribution. The LF of galaxies in a halo/cluster of fixed mass, entitled the conditional luminosity function (CLF) in the literature (Yang, Mo & van den Bosch 2003), statistically models how galaxies occupy dark matter haloes. Modelling the halo occupation distribution (HOD; Peacock & Smith 2000; Berlind & Weinberg 2002; Bullock, Wechsler & Somerville 2002) provides another popular yet closely related approach. Given a dark matter halo distribution, these models (HOD and CLF) can be linked with several galaxy distribution and evolution properties (e.g. Popesso

et al. 2005; Cooray 2006; Popesso et al. 2007; van den Bosch et al. 2007; Zheng, Coil & Zehavi 2007; Zehavi et al. 2011; Leauthaud et al. 2012; Reddick et al. 2013), including galaxy correlation functions (e.g. Jing, Mo & Börner 1998; Peacock & Smith 2000; Seljak 2000), galaxy luminosity/stellar mass functions (e.g. Yang, Mo & van den Bosch 2009), global star formation rate (e.g. Behroozi, Wechsler & Conroy 2013) and galaxy–galaxy lensing signals (e.g. Mandelbaum et al. 2006).

Furthermore, LF and HOD analyses improve our understanding of the cluster galaxy population. The number of cluster galaxies, especially the number of cluster RS galaxies, is a useful mass proxy for cluster abundance cosmology. Deep optical surveys like the Dark Energy Survey (DES,¹; DES Collaboration 2005) demand refined understanding of the evolution of cluster galaxies to $z = 1.0$ (Melchior et al. 2017).

The Sloan Digital Sky Survey (SDSS²) has enabled detailed analysis of the cluster LFs (or CLFs) with the identification of tens of thousands of clusters to redshift 0.5 (Yang, Mo & van den Bosch 2008; Hansen et al. 2009). Above redshift 0.5, most studies have been performed with relatively small samples containing a handful of clusters or groups (Andreon 2008; Crawford et al. 2009; Rudnick et al. 2009; De Propriis et al. 2013; Martinet et al. 2015; De Propriis 2017) and wide-field surveys that are more sensitive than SDSS have just provided an opportunity to reinvigorate such analyses (Sarron et al. 2018).

In this paper, we constrain the (conditional) red-sequence luminosity function (RSLF) with an X-ray selected cluster sample (details in Section 2.3) detected in the DES Science Verification (DES-SV) data including the supernovae data sets collected during the same time. Clusters selected with the same approach are used in a cluster central galaxy study in Zhang et al. (2016), but with an updated X-ray archival data set. The sample contains ~ 100 clusters and groups in the mass range from $3 \times 10^{13} M_{\odot}$ to $2 \times 10^{15} M_{\odot}$, and the redshift range of 0.1–1.05. To date, it still represents a cluster sample that is complete to the highest redshift range discovered in DES, owing to the full depth data sets collected during DES-SV. As the clusters are not selected by their RS properties, studying RSLF with the sample is not subject to red sequence selection biases. Similar analyses can also be applied to SZ-selected clusters (e.g. clusters discovered from the South Pole Telescope survey: Bleem et al. 2015; Hennig et al. 2017) and clusters selected from optical data. Our paper focuses on cluster red members. The luminosity function of blue galaxies generally deviates from that of the red, but the red cluster members are easier to select photometrically due to the tightness of the colour–magnitude relation.

The number of member galaxies in low-mass clusters is often too low to study LFs for individual systems. It is a common approach to stack the member galaxy luminosity distributions for an ensemble of clusters (e.g. Hansen et al. 2009; Yang et al. 2009). In this paper, we develop a hierarchical Bayesian modelling technique. The method allows us to acquire similar results to a stacking method, with the added benefits of robust uncertainty estimation and simultaneous quantification of the possible mass dependence and redshift evolution effects. In the rest of the paper, we first introduce our data sets in Section 2 and then describe the methods in Section 3. The results are presented in Section 4. Discussions of the methods and results as well as a summary of the paper are presented in Section 5.

¹<https://www.darkenergysurvey.org>

²<http://www.sdss.org>

2 DATA

2.1 Dark Energy Survey Science Verification data

We use the DES Science Verification (DES-SV) data taken in late 2012 and early 2013. The DES collaboration collected this data set with the newly mounted Dark Energy Camera (DECam; Flaugher et al. 2015) for science verification purposes before the main survey began (for details on DES Year 1 operations, see Diehl et al. 2014). In total, the data set covers $\sim 400 \text{ deg}^2$ of the sky. For about 200 deg^2 , data are available³ in all of the g , r , i , z , and Y bands, and the total exposure time in each band fulfils DES full depth requirement (23–24 mag in i and 22–23 mag in z , see more details in Sánchez et al. 2014). A pilot supernovae survey (see Papadopoulos et al. 2015, for an overview) of 30 deg^2 sky in g , r , i , z was conducted at the same time, reaching deeper depth after image coaddition (~ 25 mag in i and ~ 24 mag in z).

The DES-SV data are processed with the official DES data reduction pipeline (Sevilla et al. 2011; Mohr et al. 2012). In this pipeline, single exposure images are assessed, detrended, calibrated, and coadded. The coadded images are then fed to the SEXTRACTOR software (Bertin & Arnouts 1996; Bertin 2011) for object detection and photometry measurement.

2.2 The DES photometric data

We use a DES value-added catalogue, the ‘gold’ data set (see the review in Rykoff et al. 2016; Drlica-Wagner et al. 2018),⁴ based on catalogues produced from the SEXTRACTOR software. The detection threshold is set at 1.5σ ($\text{DETECT_THRESH} = 1.5$) with the default SEXTRACTOR convolution filter. The minimum detection area is set at 6 pixels⁵ ($\text{DETECT_MINAREA} = 6$). The SEXTRACTOR runs were performed in dual mode, using the linear addition of r , i , and z band images as the detection image.

The ‘gold’ data set is subsequently derived with the initial detections, keeping only regions that are available in all of the g , r , i , z bands. Regions with a high density of outlier colours due to the impact of scattered light, satellite or airplane trails, and regions with low density of galaxies near the edge of the survey are removed. Objects near bright stars selected from the Two Micron All Sky Survey (2MASS; Skrutskie et al. 2006) are masked. The masking radius scales with stellar brightness in J as $R_{\text{mask}} = 150 - 10J$ (arcsec) with a maximum of 120 arcsec (Jarvis et al. 2016; Rykoff et al. 2016). Stars of nominal masking radii less than 30 arcsec are not masked to avoid excessive masking. Coverage of the sample is recorded with the HEALPIX⁶ software (Górski et al. 2005) gridded by $N = 4096$. Photometry is re-calibrated and extinction corrected using the Stellar Locus Regression technique (SLR; Kelly et al. 2014).

We make use of the SEXTRACTOR Kron magnitudes (mag_auto , Kron 1980) for all detected objects. Since the SEXTRACTOR run was performed in dual mode, the Kron aperture and the centroid for different filters are the same, which are determined from the detection images. The luminosity functions are derived with DES z -band photometry, based on objects $>5\sigma$ (which corresponds to $\text{magerr_auto_}z < 2.5/\ln 10/5 = 0.218 \text{ mag}$).

³<http://des.ncsa.illinois.edu/releases/sva1>

⁴<https://des.ncsa.illinois.edu/releases/sva1>

⁵DECam pixel scale $0.263''$.

⁶<http://healpix.sourceforge.net>

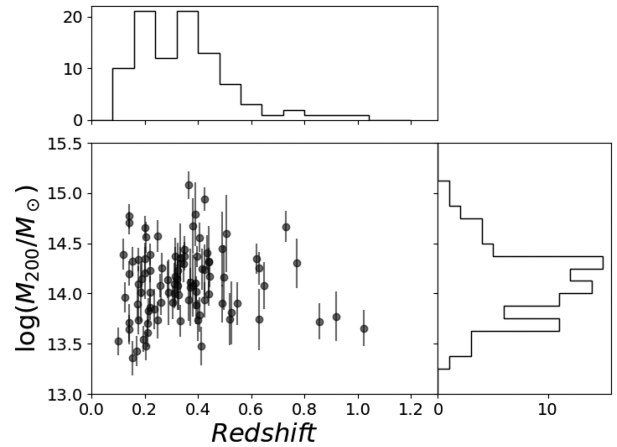


Figure 1. The XCS-SV clusters: redshifts, masses, and mass uncertainties. The upper and right histograms, respectively, show the cluster redshift and mass distribution.

We derive completeness limits for the selected $>5\sigma$ objects. Details of the completeness analyses are provided in Appendix A. In general, the completeness limits are $\sim 0.5 \text{ mag}$ brighter than the sample’s 10σ depth magnitudes. The selected $>5\sigma$ objects are >99.8 per cent complete above the limits. Because of this high completeness level, we do not correct for incompleteness in this paper.

2.3 The XCS-SV cluster sample

The XCS-SV cluster sample is a product from the *XMM* Cluster Survey (Lloyd-Davies et al. 2011; Mehtens et al. 2012; Viana et al. 2013), which searches for galaxy cluster candidates (extended X-ray emissions) in the *XMM-Newton* archival data. The X-ray selected cluster candidates (about 300 in number) are later confirmed with the DES-SV optical images, and have their photometric redshifts estimated using the DES-SV photometric data set. The XCS-SV sample contains galaxy groups, low-mass clusters and clusters as massive as $10^{15} M_{\odot}$ to beyond redshift 1. Selection and confirmation methods of the sample, as well as the cluster photometric redshift measurements are reviewed in Zhang et al. (2016, henceforth referenced as Z16). The sample used in this paper is expanded from that in Z16 after finalizing the input X-ray data. We make use of only the clusters of which the mass uncertainties, derived from the X-ray temperature measurements, are less than 0.4 dex.

Since this paper evaluates luminosity function with the z -band photometry, we eliminate clusters above redshift 1.05 for which the rest frame 4000 \AA break of RS galaxies have shifted out of DES z -band coverage (sensitive to $\sim 8500 \text{ \AA}$). We only use clusters located in DES-SV regions with the analysis magnitude ranges (above characteristic magnitude + 2 mag) above the completeness limits (Section 2.2). The paper works with 93 clusters in total, which are listed in Appendix B, Table B1. In Fig. 1, we show the redshifts, masses, and mass uncertainties of the analysed clusters.

The cluster masses and uncertainties are derived from X-ray temperature based on a literature T_X – M relation (Kettula et al. 2013) (see details also in Z16). R_{200} is derived from M_{200} .

2.4 Red-sequence galaxy selection

The definition of cluster member galaxies in projected data sets is a difficult challenge. Our method is based on simple colour cuts

around the cluster red sequence (De Lucia et al. 2007; Stott et al. 2007; Gilbank et al. 2008; Crawford et al. 2009; Martinet et al. 2015). To account for the shifting of the 4000 Å break, we select RS galaxies according to $g - r$ colour at $z < 0.375$, $r - i$ colour at $0.375 < z < 0.775$, and $i - z$ colour at $0.775 < z < 1.1$.

For a cluster at redshift z , we first apply K -corrections (Blanton & Roweis 2007) to all the objects in the cluster field. These objects are band-shifted to a reference redshift (depending on the colour choice), assuming the cluster redshift to be their original redshifts. We compare the corrected colours to a model colour with the following standard:

$$|(g - r)_{z=0.25} - (g - r)_{\text{model at } z=0.25}| < \sqrt{\delta_{g-r}^2 + \Delta_{g-r}^2}, \text{ or}$$

$$|(r - i)_{z=0.55} - (r - i)_{\text{model at } z=0.55}| < \sqrt{\delta_{r-i}^2 + \Delta_{r-i}^2}, \text{ or}$$

$$|(i - z)_{z=0.9} - (i - z)_{\text{model at } z=0.9}| < \sqrt{\delta_{i-z}^2 + \Delta_{i-z}^2}. \quad (1)$$

In these equations, the model colours ($g - r$, $r - i$, or $i - z$, details explained below) are the mid-points of a selection window at a reference redshift. δ_{g-r} , δ_{r-i} , and δ_{i-z} are the photometry uncertainties. Δ_{g-r} , Δ_{r-i} , and Δ_{i-z} are the widths of the selection windows.

We set Δ_{g-r} to be 0.2 mag. The clipping width is chosen to be larger than the combination of the intrinsic scatter and the slope of red sequence colour–magnitude relations, while avoiding a significant amount of blue galaxies. Δ_{r-i} is adjusted to be 0.15 through matching the number of selected cluster galaxies (after background subtraction, see Section 3.2 for details) to fiducial $g - r$ selections at $0.3 \leq z < 0.5$. Δ_{i-z} is adjusted to be 0.12 through matching the number of selected cluster galaxies (after background subtraction, see Section 3.2 for details) to fiducial $r - i$ selections at $z \geq 0.7$.

The model colours of $g - r$ at $z = 0.25$, $r - i$ at $z = 0.55$, and $i - z$ at $z = 0.9$ are based on a simple stellar population template from Bruzual & Charlot (2003), assuming a single star burst of metallicity $Z = 0.008$ at $z = 3.0$, computed with the EZGAL package⁷ (Mancone & Gonzalez 2012). In Fig. 2, we show the RS model, overplotting the observer frame colours of the selected objects. Overall, the colours of the selected RS candidates match template well. The template also matches the colours of cluster red sequence defined by the RedMaPPer method (Rykoff et al. 2016).

For RS candidates selected with the above criteria, we employ a statistical background subtraction approach (see details in Section 3) to eliminate background objects, which on average constitute 50 per cent of the cluster region galaxies brighter than $m^* + 2$ mag.

The performance of star-galaxy classifiers applied to the DES SVA1 ‘gold’ sample (Section 2.2) depends on the object’s apparent magnitude. The classifiers become unstable for objects fainter than ~ 22 mag in the z -band. Since it is possible to eliminate the stellar contamination with the background subtraction procedure (we estimate the background object – stellar and galactic – densities locally for each cluster), we do not attempt to separate stars and galaxies among the RS candidates (above 21 mag in z , stars make up ~ 10 per cent of the sample). We nevertheless refer to all objects as ‘galaxies’.

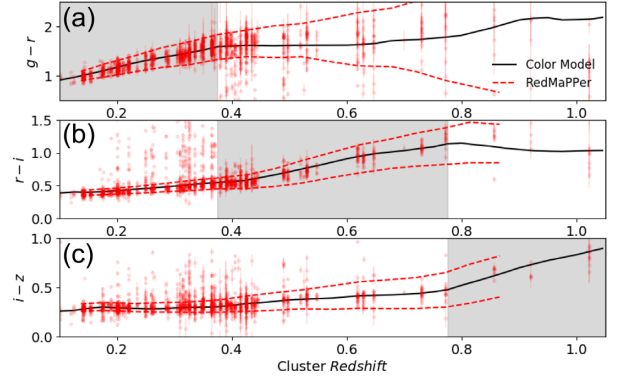


Figure 2. Observer-frame $g - r$ (panel a), $r - i$ (panel b), and $i - z$ (panel c) colours of the cluster RS candidates (red data points) and the RS model (black solid lines). Note that the colour distributions of cluster foreground/background objects are not subtracted. We also show the 2σ colour ranges of RS cluster members (member probability > 50 per cent) from the redMaPPer DES-SV cluster sample (Rykoff et al. 2016) for comparison, which appear to agree with our colour models.

3 METHODS

The main results in this paper are derived with a hierarchical Bayesian method (application examples to cosmology can be found in Lored & Hendry 2010). We constrain the RSLF with a single Schechter function (Schechter 1976) to the magnitude limit of $m_s + 2$ mag, and simultaneously model the mass and redshift dependence of the parameters (Section 3.1: a hierarchical Bayesian method). To test the method, we compare the constraints to results derived from stacking cluster galaxy number counts in luminosity bins (Section 3.2: alternative histogram method).

Generally, the input to both methods includes the observed magnitudes, $\{m_i\}$, of objects inside clusters or in a ‘field’ region (m_i is the apparent magnitude of the i th object). We define the cluster region as enclosed within $0.6 R_{200}$ of the cluster centres (X-ray centres). The contrast between cluster and background object densities is large with this choice (excess cluster object density to background object density about 1:1 for most of the clusters throughout the DES-SV depth), and the amount of retained cluster galaxies is reasonable. We choose the field region to be annular, centred on the cluster, with the inner and outer radii being $3 R_{200}$ and $8 R_{200}$, respectively. The choice helps eliminating RSLF contributions from cluster-correlated large-scale structures along the line of sight. The cluster central galaxies selected according to the criteria in Z16 are eliminated from the analysis. Central galaxies are known to be outliers to a Schechter function distribution. Their properties and halo occupation statistics are investigated in Z16.

The area of these regions are traced with randomly generated locations that have uniform surface density across the ‘gold’ sample footprint, i.e. a sample of ‘random points’. For each cluster, we generate ~ 1.5 million random points within $10 R_{200}$. The number density is high enough that the resulting uncertainty is negligible (~ 1 per cent in the luminosity distribution measurements). We ignore the uncertainties from using random points.

3.1 A hierarchical Bayesian method

Given a model with a set of parameters Ω that describes the distribution of observables, Bayesian theory provides a framework for inferring Ω with a set of observed quantities $\{x\}$.

⁷<http://www.baryons.org/ezgal/>

In this sub-section, we describe the methods developed in this framework.

Denoting the probability of observing $\{x\}$ in model Ω to be $P(\{x\}|\Omega)$, and the prior knowledge about the model parameters to be $P(\Omega)$, after observations of $\{x\}$, the Bayes' theorem updates the knowledge about model parameters, namely the posterior distribution, to be

$$P(\Omega|\{x\}) \propto P(\{x\}|\Omega)P(\Omega). \quad (2)$$

The above equation uses a proportional sign instead of an equal sign as a probability function needs to be normalized to 1. The normalization factor is un-interesting when the posterior probability is sampled with Markov Chain Monte Carlo.

In our application, the observables include the observed magnitudes of objects in the cluster or field region. A major component of our model is the Schechter function. The parameters of the Schechter function vary for clusters of different masses and redshifts. Our model, called the *hierarchical* model, assumes redshift and mass dependences for the faint end slope and the characteristic magnitude. For the parameter priors $P(\Omega)$, we assume them to be flat for most of the parameters excluding a couple. The prior distributions are noted later when we introduce the parameters.

3.1.1 Basic components of the model

For one cluster galaxy, we assume that the probability of observing it with magnitude m follows a Schechter function

$$f(x) = \psi_f(0.4\ln 10)10^{0.4(m^* - x)(\alpha + 1)} \exp(-10^{0.4(m^* - x)}). \quad (3)$$

In this equation, ψ_f is the normalization parameter that normalizes $f(x)$ to 1. α and m^* are the faint end slope and the characteristic magnitude, treated as free parameters of the model.

For one object in the cluster region, it can be either a *cluster galaxy* or a *field object*. For a field object, we denote the probability of observing it with magnitude m to be $g(m)$. $g(m)$ is approximated with a normalized histogram of the object magnitude distribution in the field region.

The probability of observing one object in the cluster region is the combination of observing it as a *field* object and observing it as a *cluster* galaxy. The probability writes

$$h(m) = \psi_h[N_{cl}f(m) + N_{bg}g(m)]. \quad (4)$$

In this equation, N_{cl} is the number of cluster galaxies in the cluster region, and N_{bg} is the number of field galaxies in the cluster region. Again, there exists a normalization factor ψ_h that normalizes the probability function to 1.

We treat the sum of N_{bg} and N_{cl} as a Poisson distribution. The expected value of N_{bg} can be extrapolated from the field region and the area ratio between the cluster and the field regions. Equation (4) introduces *one* free parameter, N_{cl} , which controls the relative density between cluster and field galaxies in the cluster region. N_{cl} can be further related to the amplitude of the Schechter function, ϕ^* (in unit of total galaxy count), as the integration of the Schechter function over the interested magnitude range, written as

$$\begin{aligned} N_{cl} &= \int \frac{\phi^* f(m)}{\psi_f} dm \\ &= \frac{\phi^*}{\psi_f} \int f(m) dm. \end{aligned} \quad (5)$$

Thus far, the free parameters in our models are α , m^* from equation (3) and ϕ^* . Note that, in this section, we only perform analyses with galaxies brighter than the completeness magnitude limit (galaxies are considered to be more than 99.8 per cent complete throughout the analysed magnitude range, according to Section A).

We constrain ϕ^* with the number count of observed objects in the cluster region (N), assuming a Poisson distribution:

$$N \sim \text{Poisson}(N_{cl} + N_{bg}). \quad (6)$$

The log likelihood is explicitly written as

$$\log \mathcal{P}(N) \propto N \log(N_{cl} + N_{bg}) - (N_{cl} + N_{bg}). \quad (7)$$

For one cluster, we take the observables to be the observed magnitudes of cluster region objects, $\{m_i\}$, the object number count and N and the background object number count. N_{bg} is treated as a known quantity. The log likelihood of observing these quantities is

$$\begin{aligned} \log \mathcal{P}(\{m_i\}, N | \alpha, m^*, \phi^*) \\ \propto \log \mathcal{P}(N | \phi^*, \alpha, m^*) + \sum_i \log \mathcal{P}(\{m_i\} | \alpha, m^*, \phi^*) \\ \propto \log \mathcal{P}(N) + \sum_i \log h(m_i). \end{aligned} \quad (8)$$

3.1.2 Hierarchical model

The Bayesian approach makes it possible to add dependences to α and m^* . We rewrite α and m^* with redshift or mass dependences

$$\alpha_j = A_\alpha \log(1 + z_j) + B_\alpha (\log M_{\text{model},j} - 14) + C_\alpha$$

$$m_{z=0.4,j}^* = B_m (\log M_{\text{model},j} - 14) + C_m. \quad (9)$$

Here, we distinguish between true and observed M_{200} of clusters. $\log M_{\text{model},j}$ represents the true M_{200} mass of the j th cluster, while we use $\log M_{\text{obs},j}$ to represent the M_{200} mass derived from X-ray temperature for the j th cluster. $\log M_{\text{model},j}$ for different clusters are treated as free parameters in the analysis, but we use observational constraints on $\log M_{200}$ from X-ray data as priors (Gaussian distributions): $\log M_{\text{model},j} \sim \mathcal{N}(\log M_{\text{obs},j}, \sigma_M^2)$. σ_M is the measurement uncertainty (including the intrinsic scatter and statistical uncertainties) of $\log M_{\text{obs},j}$ from X-ray data. The assumption about $\log M_{\text{model},j}$ allows us to incorporate mass uncertainties into the analysis. Furthermore, we constrain m^* at $z = 0.4$ (the mean and median redshifts of the sample are 0.33 and 0.35, respectively) to be consistent with the redshift cut in the alternative method in Section 3.2. For each cluster, we extrapolate the m^* at its observed z from $z = 0.4$ assuming a simple stellar population from Bruzual & Charlot (2003) with a single-star burst of metallicity $Z = 0.008$ at $z = 3.0$ (the RS galaxy template used in Section 2.4).

ϕ^* for each cluster is constrained separately. We assume a Gaussian prior distribution of $\{\log \phi_j^*\}$ given the values predicted by the relation: $\phi_j^* \sim \mathcal{N}(\log \phi_{\text{mean},j}^*, \sigma_{\log \phi}^2)$. $\sigma_{\log \phi}$ is the intrinsic scatter of the relation, fixed at 0.5⁸ to reduce the number of free parameters. We further assume a power-law relation between $M_{\text{model},j}$ and $\phi_{\text{mean},j}^*$

$$\log \phi_{\text{mean},j}^* = B_\phi \times \log M_{\text{model},j} + C_\phi. \quad (10)$$

⁸Allowing the parameter to vary gives a scatter of ~ 0.2 – 0.3 , and therefore we decided to set a value conservatively larger to avoid overconstraining the $\sigma_{\log \phi}$ parameters.

The log likelihood of having ϕ_j^* given $M_{\text{model},j}$ writes:

$$g_j(\phi_j^*) \propto -\frac{(\phi_j^* - (B_\phi \times \log M_{\text{model},j} + C_\phi))^2}{2\sigma_\phi^2}. \quad (11)$$

The free parameters of this model are $A_\alpha, B_\alpha, C_\alpha, B_m, C_m, B_\phi, C_\phi, \{\phi_j^*\}$, and $\{M_{\text{model},j}\}$. The observed quantities are $\{m_{i,j}\}$ and $\{N_j\}$ of all clusters. $\{\log M_{\text{obs},j}\}$ are treated as priors for $\{\log M_{\text{model},j}\}$. $\{z_j\}$ as well as $N_{\text{bg},j}$ are treated as known quantities for each of the clusters. We summarize the model dependences with a schematic diagram in Fig. 3. The log-likelihood of observing these quantities is:

$$\begin{aligned} \log \mathcal{L}(\{m_{i,j}\}, \{N_j\} | A_\alpha, B_\alpha, C_\alpha, B_m, C_m, B_\phi, C_\phi, \{\phi_j^*\}, \{M_{\text{model},j}\}) \\ = \log \mathcal{L}(\{m_{i,j}\}, \{N_j\} | \alpha_j, m_j^*, \{\phi_j^*\}) + \log \mathcal{L}(\{\phi_j^*\} | \{M_{\text{model},j}\}) \\ \propto \sum_j \left[\log \mathcal{P}(N_j | \phi_j^*, \alpha_j, m_j^*) + \sum_i \log \mathcal{P}(m_{i,j} | \alpha_j, m_j^*, \phi_j^*) \right] \\ + \sum_j \log \mathcal{L}(\phi_j^* | M_{\text{model},j}) \\ \propto \sum_j \left[\log \mathcal{P}_j(N_j) + \sum_i \log h_j(m_i, j) + g_j(\phi_j^*) \right]. \quad (12) \end{aligned}$$

Finally, the parameter posterior likelihood is

$$\begin{aligned} \log \mathcal{L}(A_\alpha, B_\alpha, C_\alpha, B_m, C_m, B_\phi, C_\phi, \{\phi_j^*\}, \{M_{\text{model},j}\} | \{m_{i,j}\}, \{N_j\}) \\ = \log \mathcal{L}(\{m_{i,j}\}, \{N_j\} | \alpha_j, m_j^*, \{\phi_j^*\}) + \log \mathcal{L}(\{\phi_j^*\} | \{M_{\text{model},j}\}) \\ \propto \sum_j \left[\log \mathcal{P}(N_j | \phi_j^*, \alpha_j, m_j^*) + \sum_i \log \mathcal{P}(m_{i,j} | \alpha_j, m_j^*, \phi_j^*) \right] \\ + \sum_j \log \mathcal{L}(\phi_j^* | M_{\text{model},j}) \\ + \log \mathcal{L}_{\text{prior}}(A_\alpha, B_\alpha, C_\alpha, B_m, C_m, B_\phi, C_\phi, \{\phi_j^*\}, \{M_{\text{model},j}\}) \\ \propto \sum_j \left[\log \mathcal{P}_j(N_j) + \sum_i \log h_j(m_i, j) + g_j(\phi_j^*) \right] \\ + \log \mathcal{L}_{\text{prior}}(A_\alpha, B_\alpha, C_\alpha, B_m, C_m, B_\phi, C_\phi, \{\phi_j^*\}, \{M_{\text{model},j}\}). \quad (13) \end{aligned}$$

We assume flat priors for most of the model parameters except C_m and ϕ_j . For C_m , we assume a Gaussian distribution as the prior, with the measurement from Hansen et al. (2009) as the mean, and 1 mag² as the variance. These priors are listed in Table 1. Sampling from the parameter posterior likelihood is performed with the PYMC package (Fonnesbeck et al. 2015).

3.2 Alternative histogram method

We develop a separate method to test the fore-mentioned technique. This method starts with counting galaxies in magnitude bins. We use 150 bins from 15 to 30 mag spaced by 0.1 mag. We do not see change of the results when adjusting the bin size from 0.2 to 0.05 mag.

The histogram counting is performed for the cluster region, $N(m)$, and the field region, $N(m)_{\text{background}}$. To estimate the contribution of

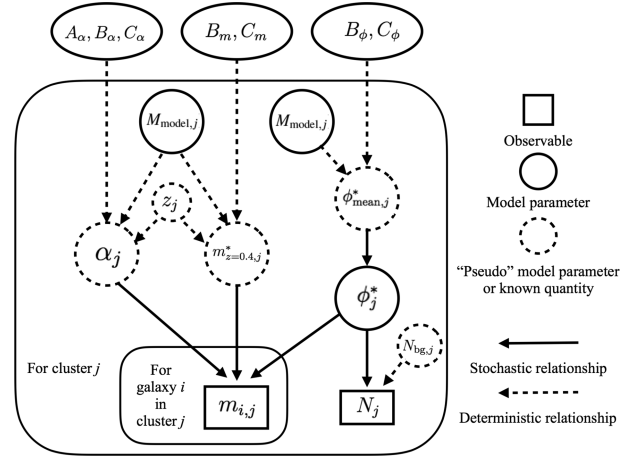


Figure 3. Schematic diagram of the hierarchical Bayesian method, as described in Section 3.1. Note that Schechter function parameters like α_j , $m_{z=0.4,j}^*$, and ϕ_j^* are not directly constrained in the model. Such ‘parameters’ (called pseudo-parameters in the diagram), as well as known quantities are indicated by dashed line circles.

Table 1. Prior and posterior distributions of the parameters (see equations 9 and 10) in the hierarchical Bayes model.

	Prior	Posterior
A_α	$[-5, 10]$	1.30 ± 0.70
B_α	$[-4, 4]$	-0.17 ± 0.19
C_α	$[-2, 2]$	-0.77 ± 0.16
B_m	$[-10, 10]$	-0.31 ± 0.31
C_m	$\mathcal{N}(-22.13, 1.0)$	-22.19 ± 0.19
at $z = 0.4$	$\mathcal{N}(19.69, 1.0)$	19.63 ± 0.19
B_ϕ	$[-5, 5]$	0.73 ± 0.13
C_ϕ	$[-10, 10]$	0.85 ± 0.08

field galaxies to the cluster histogram, we weight the number count of objects in the field region, with the random number ratio:

$$N_{\text{bg}}(m) = N(m)_{\text{background}} \times \frac{N_{\text{random, cluster}}}{N_{\text{random, background}}}. \quad (14)$$

We add up the histograms of clusters binned by redshift or cluster mass,⁹ and also record the number count of clusters in each magnitude bin, $C(m)$. During the summing process, we shift m by the apparent magnitude difference between the cluster redshift and a reference redshift (depending on the cluster redshift and mass binning) of a simple passively evolving stellar population from Bruzual & Charlot (2003) with a single-star burst of metallicity $Z = 0.008$ at $z = 3.0$ (the same RS galaxy template used in Sections 2.4 and 3.1.2). The histograms are then averaged for both the cluster region and the field region to obtain $\bar{N}(m)$ and $\bar{N}_{\text{bg}}(m)$. Subtracting $\bar{N}_{\text{bg}}(m)$ from $\bar{N}(m)$ yields the luminosity distribution of cluster galaxies (Fig. 4 in redshift bins and Fig. 5 in mass bins).

We assume a Schechter function distribution for cluster galaxies

$$S(m) = \phi(0.4 \ln 10) 10^{0.4(m^* - m)(\alpha + 1)} \exp(-10^{0.4(m^* - m)}), \quad (15)$$

⁹Two clusters are further eliminated from the 93 cluster sample because they are severely masked and therefore do not reliably contribute to the stacked histograms.

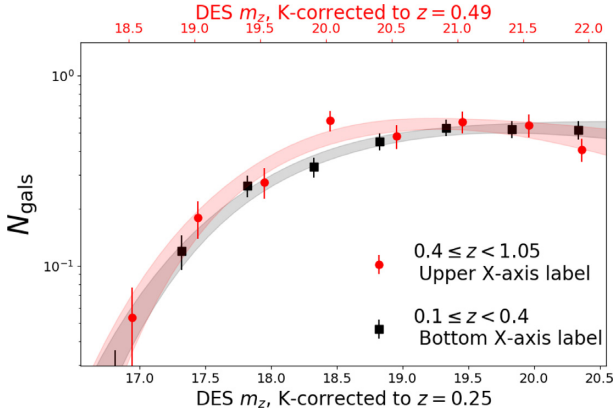


Figure 4. RSLFs derived in two redshift bins display a possible redshift evolution effect. Uncertainties with the data points are estimated through assuming Poisson distributions. The shaded bands show the fitted Schechter functions including 1σ fitting uncertainties (with the method from Section 3.2). Note that the data points have been rebinned from the input to the fitting method.

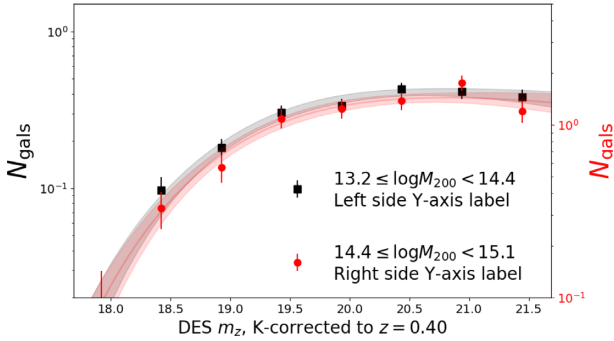


Figure 5. RSLFs derived in two cluster mass bins appear to be consistent. Uncertainties with the data points are estimated through assuming Poisson distributions. The shaded bands show the fitted Schechter functions including the 1σ fitting uncertainties (with the method from Section 3.2). Note that the data points have been rebinned from the input to the fitting method.

therefore the expected number of galaxies in each magnitude bin in the cluster region is

$$E(m) = S(m) + N_{bg}(m). \quad (16)$$

Assuming Poisson distributions for the number of galaxies in each bin, we sample from the following likelihood:

$$\log \mathcal{L} \propto \sum_m \bar{N}(m) C(m) \log[E(m) C(m)] - E(m) C(m). \quad (17)$$

Sampling from the likelihood is performed with the EMCEE package (Foreman-Mackey et al. 2013).

4 RESULTS

4.1 Results from hierarchical Bayesian modelling

The hierarchical Bayes model (Section 3.1.2) simultaneously constrains the redshift evolution and mass dependence of α and m_* anchored at redshift 0.4

$$\begin{aligned} \alpha &= A_\alpha \log(1+z) + B_\alpha (\log M_{200} - 14) + C_\alpha \\ m_{z=0.4}^* &= B_m (\log M_{200} - 14) + C_m. \end{aligned} \quad (18)$$

The m_* at other redshifts are derived through evolving a passive redshift evolution model described in Section 3.1.2.

For each cluster, we only make use of the $[m^* - 2, m^* + 2]$ magnitude range. Galaxy members of the analysed clusters are complete within this range by selection (see details in Section 2.3). The constraints of the α and m_z^* relations are listed in Table 1. The model posterior distributions are Gaussian-like according to visual checks. In Fig. 6, we plot the α and m_z^* relations as well as their uncertainties. For comparison, we show constraints from the alternative histogram approach (discussed in the following section).

The RSLF faint end slope, α , displays a weak evidence of redshift evolution. The A_α parameter that controls the redshift evolution effect deviates from 0 at a significance level of 1.9σ . For clusters of $\log M_{200} = 14.1$ (median mass of the cluster sample), α is constrained to be -0.69 ± 0.13 at $z = 0.2$, rising to -0.52 ± 0.14 at $z = 0.6$. The mass dependence of α is ambiguous. The B_α parameter that controls this feature deviates from 0 by 0.9σ . The effect is likely degenerate with the mass dependence of m^* . When removing m^* mass dependence from the method (setting B_m to be 0), B_α is consistent with 0.

We assume passive evolution to the RSLF characteristic magnitude m_z^* . We do not notice deviations of m^* from the assumption (the m^* results in redshift and mass bins agree with the model). Although the method models m^* as mass-dependent, the effect appears to be insignificant (B_m deviates from 0 by 1.0σ).

The hierarchical Bayesian method also constrains the RSLF amplitudes, ϕ^* , and the relations between ϕ^* and $\log M_{200}$. ϕ^* scales with the total number of cluster galaxies. Our result shows a strong correlation between ϕ^* and the cluster mass (Fig. 7).

4.2 Results in redshift/mass bins

We divide the clusters into two redshift bins: $0.1 \leq z < 0.4$ and $0.4 \leq z < 1.05$ and apply the alternative histogram method (Section 3.2).¹⁰ The median cluster masses in each of the bins are $10^{14.1}$ and $10^{14.16} M_\odot$, respectively. The fitted parameters are listed in Table 2. Results are also shown in Figs 4 and 6. Again, the RSLF faint end slope, α , displays a hint of redshift evolution. The measurements in two redshift bins differ by $\sim 1.2\sigma$.

We divide the clusters into two mass bins: $13.2 \leq \log M_{200} < 14.4$, $14.4 \leq \log M_{200} < 15.1$, and apply the alternative histogram method. The median cluster redshifts in each of the bins are 0.35 and 0.34, respectively. To reduce uncertainties from band-shifting, we K -correct the RSLFs to $z = 0.4$ (based on the RS model in Section 2.4). Results are presented in Table 2, Figs 5 and 6. No mass dependence of either α or m^* is noted.

As shown in Fig. 6, the results in cluster redshift/mass bins agree with the extrapolations from the hierarchical Bayesian model (Section 4.1) within 1σ .

4.3 Comparison to literature

In Fig. 6, we overplot literature measurements of the RSLF α and m^* parameters. In the comparison data sets, Andreon (2008), Rudnick et al. (2009), Crawford et al. (2009), De Propriis et al. (2013), and Martinet et al. (2015) utilize smaller ($N_{\text{clus}} = 5\text{--}40$) samples with individually measured LFs. For these, we compare to their stacked

¹⁰The reshift/mass cuts of the histogram samples are chosen by judgement to enlarge the redshift/mass differences of the subsets.

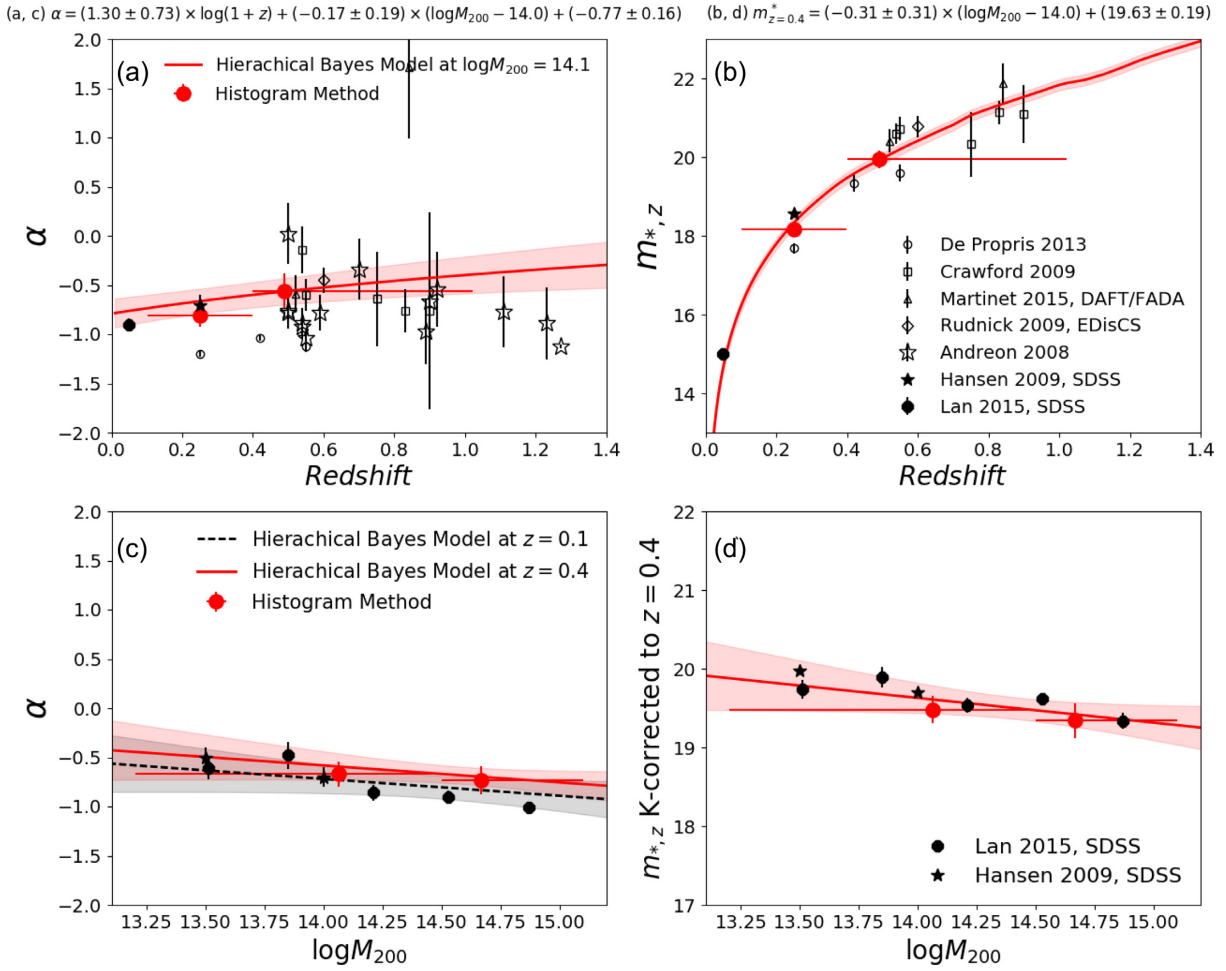


Figure 6. (Panels a and b) Redshift evolution of the faint end slope, α , and the characteristic magnitude, m^* [assuming passive redshift evolution of a simple stellar population from Bruzual & Charlot (2003) with a single star burst of metallicity $Z = 0.008$ at $z = 3.0$]. (Panels c and d) Mass dependence of the faint end slope, α , and the characteristic magnitude, m^* (assuming passive redshift evolution). Solid red lines and shades indicate results derived with the hierarchical Bayesian method (Section 3.1). Solid red circles indicate results derived with the alternative histogram method (Section 3.2). Literature reports of the α and m^* parameters are overplotted.

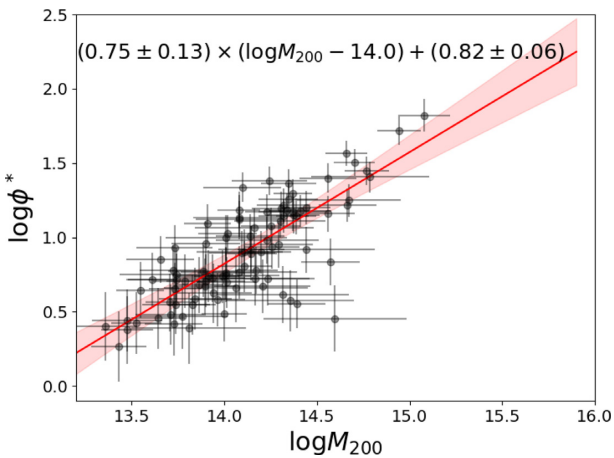


Figure 7. Constraints of the RSLF amplitudes for individual clusters (black points). We model the RSLF amplitudes as mass dependent in the hierarchical Bayesian method (Section 3.1.2). The solid line and shade show the constrained linear relation between $\log \phi^*$ and $\log M_{200}$ as well as the 1σ uncertainty (intrinsic scatter of the relations is not constrained and hence not included in the uncertainty estimation).

Table 2. Fitted Schechter function parameters in redshift/mass bins.

Cluster selection	α	m^*
$0.1 \leq z < 0.4$	-0.80 ± 0.12	18.17 ± 0.18
64 clusters		K -corrected to $z = 0.25$
$0.4 \leq z < 1.05$	-0.55 ± 0.18	19.96 ± 0.23
27 clusters		K -corrected to $z = 0.49$
$13.2 \leq \log M_{200} < 14.4$	-0.67 ± 0.12	19.48 ± 0.17
77 clusters		K -corrected to $z = 0.4$
$14.4 \leq \log M_{200} < 15.1$	-0.73 ± 0.14	19.34 ± 0.22
14 clusters		K -corrected to $z = 0.4$

analyses when available since stacking reduce intrinsic cluster-to-cluster variations, something we achieve naturally in our Bayesian hierarchical model. We note that our Bayesian analysis utilizes a likelihood that is continuous in redshift, negating the need to stack our clusters in redshift bins (see Section 3.1). We also include two low-redshift constraints from stacked RSLFs on large cluster samples from the SDSS (Hansen et al. 2009; Lan et al. 2016). We do not compare to individual cluster RSLFs from the literature, since

we do not have any known expectations on the cluster-to-cluster scatter in individual systems.

At low redshift, RSLF analyses based on SDSS data are available from Hansen et al. (2009, $z \sim 0.25$) and Lan et al. (2016, $z < 0.05$). The SDSS faint end slope measurements (Hansen et al. 2009) appear to be consistent with our results. The SDSS characteristic magnitudes appear to be slightly fainter than the values constrained in this paper, but still consistent within this paper's 1σ uncertainties (M_z^* at redshift 0.4 is -22.0 from Lan et al. or -22.13 from Hansen et al. comparing to -22.19 ± 0.19 in this paper). Note that the SDSS results are derived with r ($z < 0.05$, Lan et al. 2016) or i ($z < 0.05$, Lan et al. 2016) band data and we assume an RS model in Section 2.4 when comparing the characteristic magnitudes.

In terms of the parameter mass dependence, the α and m^* measurements from Lan et al. (2016, $z < 0.05$) in different cluster mass ranges match well with our constraints. In Hansen et al. (2009), the mass dependence results for cluster RS galaxies are not explicitly listed, but there is a trend of α steepening in the mass range of $[10^{13} M_\odot, 10^{14} M_\odot]$, and then stabilizing beyond $10^{14} M_\odot$. The quantity m^* displays a trend of brightening in the mass range of $[10^{13} M_\odot, 5 \times 10^{14} M_\odot]$, and then stabilizing beyond $5 \times 10^{14} M_\odot$. These measurements qualitatively agree to our result.

At intermediate to high redshift, measurements of RSLF are still scarce. Sample sizes used in previous works are much smaller than those in SDSS-based studies. Any mass-dependent effect of α would make it difficult to make a direct comparison in Fig. 6. Andreon (2008) measures individual LFs for 16 clusters at $z > 0.5$, which we include on Figs 6(a),(b). We caution that comparing our results to these data is problematic for two reasons. First, the Andreon (2008) clusters have RSLFs measured using galaxy data extracted from a fixed observed angle that corresponds to a smaller projected radii than we use. We utilize a fixed co-moving radius, thus minimizing any radial evolution that might be present. Secondly, our Bayesian RSLF technique smooths out cluster-to-cluster scatter, similar to stacking. On the other hand, interpreting individual cluster RSLFs requires that the specific (and small) sample be representative of the mean population. A closer comparison to our data set is to Martinet et al. (2015). They create two stacked clusters, one based on about a dozen clusters at $\langle z \rangle = 0.5$ and one based on 3 or 4 clusters at $\langle z \rangle = 0.84$. They use a fixed 1Mpc radius for their galaxy extraction. We find good agreement, although their error bars are much larger.

Our sample makes a significant contribution to the observed evolution of the RSLF through its quality, size, redshift coverage, and mass range. Compared to current RSLF analyses, our DES/XCS sample is one of the very few that we can expect cluster-to-cluster variations to be minimized over a large redshift range of $0.2 \leq z \leq 1$. We are able to constrain the RSLF over the entire redshift range without combining disparate results at different redshifts. With a single data set, we eliminate issues that could be created by heterogeneity from instrumentation, photometry, statistical techniques, etc. At the same time, by having X-ray inferred cluster masses, we are able to account for covariance in slope evolution between redshift and cluster mass.

5 DISCUSSION AND SUMMARY

This paper constrains the evolution of the red-sequence luminosity function (RSLF). Typically, the cluster LF has been studied using clusters with well-sampled data (i.e. deep observations) or through stacking/averaging clusters (Andreon 2008; Yang et al. 2008; Crawford et al. 2009; Hansen et al. 2009; Rudnick et al. 2009; De Propriis et al. 2013; Martinet et al. 2015). While our DES

observations are fairly deep, we utilize stringent completeness limits in order to avoid any complications with modelling the faint end slope. This means that the data on any individual cluster may not be good enough to measure the RSLF with traditional statistical techniques, especially at high z . At the same time, stacking has its own concerns. Crawford et al. (2009) discussed possible caveats when interpreting stacked LFs. For instance, cluster LF stacks could be biased by clusters that have brighter m_* or more negative α . Thus, the interpretation of the stacked m_* and α is complicated.

In this paper, we bridge the gap between the above two standard RSLF techniques by employing a hierarchical Bayesian model. This model allows us to use the sparse and noisy data from the individual clusters, while at the same time incorporating prior information (e.g. from the X-ray inferred cluster masses). We develop a model which allows the faint-end slope of the RSLF (parametrized as α) to be a function of the log of both the cluster mass and redshift. The model also allows m^* and the overall RSLF amplitude ϕ^* to vary linearly with the log of the cluster mass.

Using this hierarchical Bayesian model on a sample of 94 X-ray select clusters to a $z = 1.05$, we find weak (1.9σ) evidence of redshift evolution for the RSLF faint end slope. Redshift evolution in the shape of the RSLF could indicate a rising abundance of faint RS galaxies over time. The result is consistent with a non-evolving fraction of cluster red galaxies to $z \sim 1$ in clusters. For consistency, we bin the clusters according to redshift and mass and stack the RS galaxies to increase the signal to noise of the RSLF. The stacked RSLF parameters are consistent with the Bayesian results. Our work represents one of the largest RSLF studies to date that goes to redshift ~ 1.0 .

A particularly interesting by-product of this study is that our model allows us to improve the cluster mass estimation. This is because our Bayesian model allows cluster mass estimation, $\log M_{\text{model}}$, to deviate from its prior values inferred from X-ray measurements ($\log M_{\text{obs}}$) by considering the correlation between ϕ^* and cluster mass. While the posterior values of cluster mass agree to its prior values ($\log M_{\text{model}}$ compared to $\log M_{\text{obs}}$ in the top panel of Fig. 8), the precision of the mass estimations has been improved as indicated by their smaller posterior uncertainties [$\sigma(\log M_{\text{model}})$ compared to $\sigma(\log M_{\text{obs}})$ in the middle panel of Fig. 8]. The improvements are especially noticeable when the mass prior uncertainties – $\sigma(\log M_{\text{obs}})$, which include both the intrinsic scatter of the X-ray observable-mass scaling relations and statistical uncertainties of the observable – is higher than 0.3 dex.

Based on the improved estimation on the values of $\log M_{\text{model}}$, and assuming ϕ^* and X-ray measurements contribute independent Gaussian-like intrinsic and measurement uncertainties to $\log M_{\text{model}}$,

$$\frac{1}{\sigma^2(\log M_{\text{obs}})} + \frac{1}{\sigma^2(\log M_{\text{model}}) \text{ from } \phi^*} = \frac{1}{\sigma^2(\log M_{\text{model}})}, \quad (19)$$

we estimate the uncertainties of inferring cluster mass from only ϕ^* as

$$\sigma(\log M_{\text{model}}) \text{ from } \phi^* = \frac{\sigma(\log M_{\text{model}})}{\sqrt{1.0 - \frac{\sigma^2(\log M_{\text{model}})}{\sigma^2(\log M_{\text{obs}})}}}. \quad (20)$$

These estimations are shown in the bottom panel of Fig. 8, which range from 0.2 to 0.4, with an average of 0.34. Because estimating cluster mass from ϕ^* is physically driven by the cluster galaxy over densities and thus sensitive to the presence of foreground and background galaxies, these mass uncertainties tends to be much larger than the X-ray temperature derived mass uncertainties. Comparatively, optical mass proxies derived from the numbers of

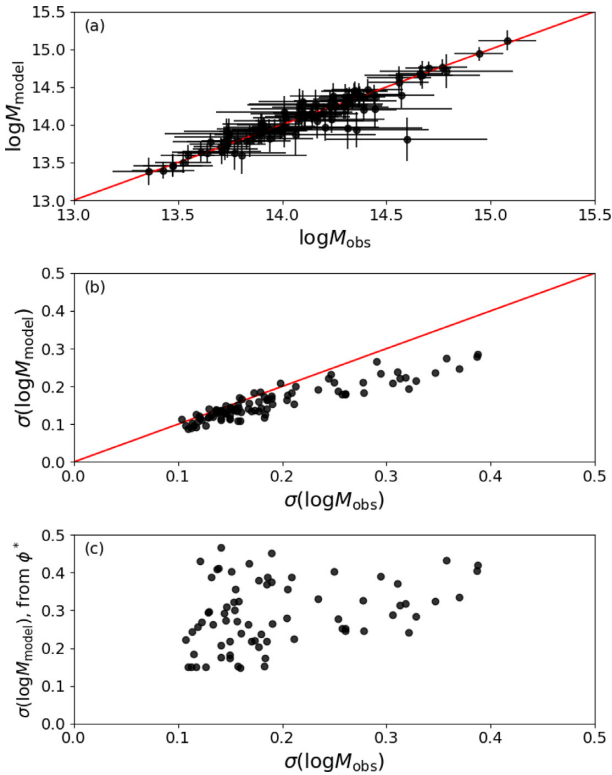


Figure 8. In the hierarchical Bayesian method, we constrain cluster masses using X-ray temperature-inferred measurements as priors. (Panel a) The posterior estimations of cluster masses, $\log M_{\text{model}}$, agree with the priors $\log M_{\text{obs}}$. (Panel b) The assumption in the hierarchical Bayes model that cluster masses scale with RSLF amplitudes, ϕ^* , helps improving the accuracy of cluster mass estimations. The posterior uncertainties of the mass estimations, $\sigma(\log M_{\text{model}})$, appear to be decreased, especially when the prior uncertainties, $\sigma(\log M_{\text{obs}})$, are higher than 0.2 dex. (Panel c) Based on the improved estimation on the values of cluster mass ($\log M_{\text{model}}$) we estimate the uncertainties of inferring cluster masses from ϕ^* only, which range from 0.2 to 0.4 dex (see details in Section 4.1).

cluster galaxies have intrinsic mass scatters between 0.2 and 0.5 dex (Rozo et al. 2009; Saro et al. 2015). This analysis demonstrates the potential of ϕ^* as a cluster mass proxy.

Since the redshift evolution of the RSLF is only insignificantly detected at a significance level of 1.9σ , it is worthwhile to apply the analysis to a larger cluster sample. We expect the XCS to find over 1000 clusters within the DES final data release. We may also utilize new and large optical cluster catalogues such as RedMaPPer. However, optically characterized clusters will add new challenges from the covariance between the richness-inferred cluster masses and the RSLFs. An evolving abundance of faint RS galaxies will also introduce a redshift evolution component into the cluster mass–richness scaling relation. Assuming the α evolution reported in this paper, we expect the number of RS galaxies above $m^* + 2$ mag to decrease by ~ 20 per cent from $z = 0$ to $z = 1.0$. Using the parameterization of cluster mass–richness scaling relation in Melchior et al. (2017), we expect the mass-to-richness ratio to change with redshift as $(1+z)^{0.26}$ [constrained as $(1+z)^{0.18 \pm 0.75(\text{stat}) \pm 0.24(\text{sys})}$ in the fore-mentioned weak lensing study]. Of course there could be additional effects on the mass–richness relation if there is redshift evolution in m^* and ϕ^* or if the mass dependence of the RSLF is not properly accounted for.

Regardless, we expect to increase the X-ray cluster sample size by at least a factor of 10 by the end of DES, covering a similar redshift range with this analysis. Using catalogue-level simulations of RSLF similar to the ones observed here, we expect to increase our sensitivity on the evolution of α by a factor of three.

If there is redshift evolution in the faint-end slope of the RS galaxies, we can explain it through the formation times and growth histories of galaxies. For instance, bright and faint cluster RS galaxies may have different formation times. It is possible that fainter galaxies are quenched during, rather than before, the cluster infall process. Hence the fraction of faint RS galaxies gradually increase with time. Astrophysical processes that slowly shut down galaxy star formation activities, e.g. strangulation (sometimes called starvation) (Larson, Tinsley & Caldwell 1980; Balogh & Morris 2000; Balogh, Navarro & Morris 2000; Peng, Maiolino & Cochrane 2015) and hence gradually increase the fraction of faint RS galaxies, will be preferred over more rapid processes such as ram-pressure stripping (Gunn & Gott 1972; Quilis, Moore & Bower 2000). Combining the observational constraints on the evolution of the faint-end slope together with the cluster accretion history in simulations should help us place good constraints on the formation and transition times of cluster RS galaxies (McGee et al. 2009).

In summary, we constrain the relation between RSLF amplitudes and cluster masses, and the correlation improves the estimation of cluster masses. We find a hint that the Schechter function faint-end slope becomes less negative for clusters at higher redshifts, indicating a rising abundance of faint RS galaxies with time. The redshift evolution of RSLF parameters may also impact the accuracy of optical cluster cosmology analyses. These results are acquired with a hierarchical Bayesian method, which has the advantage of disentangling simultaneous RSLF dependence on cluster mass and redshift despite the small size of the sample. The significance of the results would have been easily overlooked by a stacking method, which is also tested in this paper.

ACKNOWLEDGEMENTS

C. Miller as well as Y. Zhang acknowledges support from Department of Energy grant DE-SC0013520. Y. Zhang thanks Alex Drlica-Wagner, Gary Bernstein, and Chris Davis for careful reading of the draft. We use DES Science Verification in this paper. We are grateful for the extraordinary contributions of our CTIO colleagues and the DECam Construction, Commissioning and Science Verification teams in achieving the excellent instrument and telescope conditions that have made this work possible. The success of this project also relies critically on the expertise and dedication of the DES Data Management group.

Funding for the DES Projects has been provided by the U.S. Department of Energy, the U.S. National Science Foundation, the Ministry of Science and Education of Spain, the Science and Technology Facilities Council of the United Kingdom, the Higher Education Funding Council for England, the National Center for Supercomputing Applications at the University of Illinois at Urbana-Champaign, the Kavli Institute of Cosmological Physics at the University of Chicago, the Center for Cosmology and Astro-Particle Physics at the Ohio State University, the Mitchell Institute for Fundamental Physics and Astronomy at Texas A&M University, Financiadora de Estudos e Projetos, Fundação Carlos Chagas Filho de Amparo à Pesquisa do Estado do Rio de Janeiro, Conselho Nacional de Desenvolvimento Científico e Tecnológico and the Ministério da Ciência, Tecnologia e Inovação, the Deutsche

Forschungsgemeinschaft and the Collaborating Institutions in the Dark Energy Survey.

The Collaborating Institutions are Argonne National Laboratory, the University of California at Santa Cruz, the University of Cambridge, Centro de Investigaciones Energéticas, Medioambientales y Tecnológicas-Madrid, the University of Chicago, University College London, the DES-Brazil Consortium, the University of Edinburgh, the Eidgenössische Technische Hochschule (ETH) Zürich, Fermi National Accelerator Laboratory, the University of Illinois at Urbana-Champaign, the Institut de Ciències de l'Espai (IEEC/CSIC), the Institut de Física d'Altes Energies, Lawrence Berkeley National Laboratory, the Ludwig-Maximilians Universität München and the associated Excellence Cluster Universe, the University of Michigan, the National Optical Astronomy Observatory, the University of Nottingham, The Ohio State University, the University of Pennsylvania, the University of Portsmouth, SLAC National Accelerator Laboratory, Stanford University, the University of Sussex, Texas A&M University, and the OzDES Membership Consortium.

Based in part on observations at Cerro Tololo Inter-American Observatory, National Optical Astronomy Observatory, which is operated by the Association of Universities for Research in Astronomy (AURA) under a cooperative agreement with the National Science Foundation.

The DES data management system is supported by the National Science Foundation under Grant Numbers AST-1138766 and AST-1536171. The DES participants from Spanish institutions are partially supported by MINECO under grants AYA2015-71825, ESP2015-88861, FPA2015-68048, SEV-2012-0234, SEV-2016-0597, and MDM-2015-0509, some of which include ERDF funds from the European Union. IFAE is partially funded by the CERCA program of the Generalitat de Catalunya. Research leading to these results has received funding from the European Research Council under the European Union's Seventh Framework Program (FP7/2007-2013) including ERC grant agreements 240672, 291329, and 306478. We acknowledge support from the Australian Research Council Centre of Excellence for All-sky Astrophysics (CAAS-TRO), through project number CE110001020.

This manuscript has been authored by Fermi Research Alliance, LLC under Contract No. DE-AC02-07CH11359 with the U.S. Department of Energy, Office of Science, Office of High Energy Physics. The United States Government retains and the publisher, by accepting the article for publication, acknowledges that the United States Government retains a non-exclusive, paid-up, irrevocable, world-wide license to publish or reproduce the published form of this manuscript, or allow others to do so, for United States Government purposes.

REFERENCES

- Allen S. W., Evrard A. E., Mantz A. B., 2011, *ARA&A*, 49, 409
 Andreon S., 2008, *MNRAS*, 386, 1045
 Balogh M. L., Morris S. L., 2000, *MNRAS*, 318, 703
 Balogh M. L., Navarro J. F., Morris S. L., 2000, *ApJ*, 540, 113
 Behroozi P. S., Wechsler R. H., Conroy C., 2013, *ApJ*, 770, 57
 Bergé J., Gamper L., Réfrégier A., Amara A., 2013, *Astron. Comput.*, 1, 23
 Berlind A. A., Weinberg D. H., 2002, *ApJ*, 575, 587
 Bertin E., 2011, in Evans I. N., Accomazzi A., Mink D. J., Rots A. H., eds, ASP Conf. Ser. Vol. 442, *Astronomical Data Analysis Software and Systems XX*. Astron. Soc. Pac., San Francisco, p. 435
 Bertin E., Arnouts S., 1996, *A&AS*, 117, 393
 Blanton M. R., Roweis S., 2007, *AJ*, 133, 734
 Bleem L. E. et al., 2015, *ApJS*, 216, 27
 Boselli A., Gavazzi G., 2014, *A&AR*, 22, 74
 Bower R. G., Lucey J. R., Ellis R. S., 1992, *MNRAS*, 254, 589
 Bruzual G., Charlot S., 2003, *MNRAS*, 344, 1000
 Bullock J. S., Wechsler R. H., Somerville R. S., 2002, *MNRAS*, 329, 246
 Capozzi D., Collins C. A., Stott J. P., 2010, *MNRAS*, 403, 1274
 Cerulo P. et al., 2016, *MNRAS*, 457, 2209
 Chang C. et al., 2015, *ApJ*, 801, 73
 Connor T. et al., 2017, *ApJ*, 848, 37
 Cooray A., 2006, *MNRAS*, 365, 842
 Crawford S. M., Bershadsky M. A., Hoessel J. G., 2009, *ApJ*, 690, 1158
 de Filippis E., Paolillo M., Longo G., La Barbera F., de Carvalho R. R., Gal R., 2011, *MNRAS*, 414, 2771
 De Lucia G. et al., 2007, *MNRAS*, 374, 809
 De Propriis R., 2017, *MNRAS*, 465, 4035
 De Propriis R., Phillipps S., Bremer M. N., 2013, *MNRAS*, 434, 3469
 De Propriis R., Bremer M. N., Phillipps S., 2015, *MNRAS*, 450, 1268
 De Propriis R., Bremer M. N., Phillipps S., 2016, *MNRAS*, 461, 4517
 DeRose J. et al., 2019, preprint ([arXiv:1901.02401](https://arxiv.org/abs/1901.02401))
 DES Collaboration, 2005, preprint ([astro-ph/0510346](https://arxiv.org/abs/astro-ph/0510346))
 Diehl H. T. et al., 2014, in Peck A. B., Benn C. R., Seaman R. L., eds, Proc. SPIE Conf. Ser. Vol. 9149, *Observatory Operations: Strategies, Processes, and Systems V*. SPIE, Bellingham, p. 9149
 Drlica-Wagner A. et al., 2018, *ApJS*, 235, 33
 Eisenhardt P. R. M. et al., 2008, *ApJ*, 684, 905
 Faber S. M. et al., 2007, *ApJ*, 665, 265
 Flaugher B. et al., 2015, *AJ*, 150, 150
 Fönnesbeck C., Patil A., Huard D., Salvatier J., 2015, *Astrophysics Source Code Library*. record ascl:1506.005
 Foreman-Mackey D., Hogg D. W., Lang D., Goodman J., 2013, *PASP*, 125, 306
 Gilbank D. G., Yee H. K. C., Ellingson E., Gladders M. D., Loh Y.-S., Barrientos L. F., Barkhouse W. A., 2008, *ApJ*, 673, 742
 Gladders M. D., Yee H. K. C., 2000, *AJ*, 120, 2148
 Gobat R. et al., 2011, *A&A*, 526, A133
 Górski K. M., Hivon E., Banday A. J., Wandelt B. D., Hansen F. K., Reinecke M., Bartelmann M., 2005, *ApJ*, 622, 759
 Grützbauch R., Bauer A. E., Jørgensen I., Varela J., 2012, *MNRAS*, 423, 3652
 Gunn J. E., Gott J. R., III, 1972, *ApJ*, 176, 1
 Hansen S. M., Sheldon E. S., Wechsler R. H., Koester B. P., 2009, *ApJ*, 699, 1333
 Hennig C. et al., 2017, *MNRAS*, 467, 4015
 Hilton M. et al., 2009, *ApJ*, 697, 436
 Jaffé Y. L., Aragón-Salamanca A., De Lucia G., Jablonka P., Rudnick G., Saglia R., Zaritsky D., 2011, *MNRAS*, 410, 280
 Jarvis M. et al., 2016, *MNRAS*, 460, 2245
 Jing Y. P., Mo H. J., Börner G., 1998, *ApJ*, 494, 1
 Kelly P. L. et al., 2014, *MNRAS*, 439, 28
 Kettula K. et al., 2013, *ApJ*, 778, 74
 Koester B. P. et al., 2007, *ApJ*, 660, 221
 Kron R. G., 1980, *ApJS*, 43, 305
 Kurk J. et al., 2009, *A&A*, 504, 331
 Lan T.-W., Ménard B., Mo H., 2016, *MNRAS*, 459, 3998
 Larson R. B., Tinsley B. M., Caldwell C. N., 1980, *ApJ*, 237, 692
 Leauthaud A. et al., 2012, *ApJ*, 744, 159
 Leistedt B. et al., 2016, *ApJS*, 226, 24
 Lin Y.-T. et al., 2017, *ApJ*, 851, 139
 Lloyd-Davies E. J. et al., 2011, *MNRAS*, 418, 14
 Loredó T. J., Hendry M. A., 2010, *Bayesian Multilevel Modelling of Cosmological Populations*. Cambridge University Press, Cambridge, p. 245
 Mancone C. L., Gonzalez A. H., 2012, *PASP*, 124, 606
 Mandelbaum R., Seljak U., Kauffmann G., Hirata C. M., Brinkmann J., 2006, *MNRAS*, 368, 715
 Martinet N. et al., 2015, *A&A*, 575, A116
 McGee S. L., Balogh M. L., Bower R. G., Font A. S., McCarthy I. G., 2009, *MNRAS*, 400, 937

- Mehrtens N. et al., 2012, *MNRAS*, 423, 1024
 Mei S. et al., 2006, *ApJ*, 644, 759
 Melchior P. et al., 2017, *MNRAS*, 469, 4899
 Miller C. J. et al., 2005, *AJ*, 130, 968
 Mohr J. J. et al., 2012, in Radziwill N. M., Chiozzi G., eds, Proc. SPIE Conf. Ser. Vol. 8451, Software and Cyberinfrastructure for Astronomy II. SPIE, Bellingham, p. 8451
 Mullis C. R., Rosati P., Lamer G., Böhringer H., Schwöpe A., Schuecker P., Fassbender R., 2005, *ApJ*, 623, L85
 Oguri M. et al., 2018, *PASJ*, 70, S20
 Papadopoulos A. et al., 2015, *MNRAS*, 449, 1215
 Papovich C. et al., 2010, *ApJ*, 716, 1503
 Peacock J. A., Smith R. E., 2000, *MNRAS*, 318, 1144
 Peng Y., Maiolino R., Cochrane R., 2015, *Nature*, 521, 192
 Popesso P., Böhringer H., Romaniello M., Voges W., 2005, *A&A*, 433, 415
 Popesso P., Biviano A., Böhringer H., Romaniello M., 2007, *A&A*, 464, 451
 Quilis V., Moore B., Bower R., 2000, *Science*, 288, 1617
 Reddick R. M., Wechsler R. H., Tinker J. L., Behroozi P. S., 2013, *ApJ*, 771, 30
 Rozo E. et al., 2009, *ApJ*, 699, 768
 Rudnick G. et al., 2009, *ApJ*, 700, 1559
 Rykoff E. S. et al., 2012, *ApJ*, 746, 178
 Rykoff E. S. et al., 2016, *ApJS*, 224, 1
 Sánchez C. et al., 2014, *MNRAS*, 445, 1482
 Saro A. et al., 2015, *MNRAS*, 454, 2305
 Sarron F., Martinet N., Durret F., Adami C., 2018, *A&A*, 613, A67
 Schechter P., 1976, *ApJ*, 203, 297
 Seljak U., 2000, *MNRAS*, 318, 203
 Sevilla I. et al., 2011, preprint (arXiv:1109.6741)
 Skrutskie M. F. et al., 2006, *AJ*, 131, 1163
 Stanford S. A. et al., 2005, *ApJ*, 634, L129
 Stott J. P., Smail I., Edge A. C., Ebeling H., Smith G. P., Kneib J.-P., Pimbblet K. A., 2007, *ApJ*, 661, 95
 Suchyta E. et al., 2016, *MNRAS*, 457, 786
 Tanaka M. et al., 2013, *PASJ*, 65, 17
 van den Bosch F. C. et al., 2007, *MNRAS*, 376, 841
 Viana P. T. P. et al., 2013, *Astron. Nachr.*, 334, 462
 Weinberg D. H., Mortonson M. J., Eisenstein D. J., Hirata C., Riess A. G., Rozo E., 2013, *Phys. Rep.*, 530, 87
 Wen Z. L., Han J. L., 2015, *MNRAS*, 448, 2
 Yang X., Mo H. J., van den Bosch F. C., 2003, *MNRAS*, 339, 1057
 Yang X., Mo H. J., van den Bosch F. C., 2008, *ApJ*, 676, 248
 Yang X., Mo H. J., van den Bosch F. C., 2009, *ApJ*, 695, 900
 Zarattini S. et al., 2015, *A&A*, 581, A16
 Zehavi I. et al., 2011, *ApJ*, 736, 59
 Zenteno A. et al., 2011, *ApJ*, 734, 3
 Zheng Z., Coil A. L., Zehavi I., 2007, *ApJ*, 667, 760
 Zhang Y. et al., 2016, *ApJ*, 816, 98

APPENDIX A: COMPLETENESS FUNCTION

A1 The completeness function model

The completeness function models the detection probability of objects in terms of their apparent magnitude. In this paper, the completeness function is defined as the ratio between the numbers of observed and true objects at magnitude m .

We model the completeness function with a complementary error function (Zenteno et al. 2011) of three parameters:

$$p(m) = \lambda \frac{1}{2} \operatorname{erfc} \left(\frac{m - m_{50}}{\sqrt{2}w} \right). \quad (\text{A1})$$

In the above equation, m_{50} is the 50 per cent completeness magnitude, w controls the steepness of the detection drop-out rate

and λ is the overall amplitude of the completeness function. We further assume linear dependence of m_{50} and w on the depth of the image, which is characterized by the 10σ limiting magnitude.¹¹ In this paper, we evaluate the z -band completeness function, which is related to image depth in z .

A2 Relations between model parameters and image depth

The $m_{50} - m_{10\sigma}$ and $w - m_{10\sigma}$ relations are evaluated with simulated DES images and real data. The relations used in this paper are derived from the UFIG simulation (Bergé et al. 2013; Chang et al. 2015, also see Leistedt et al. 2016, for an application), which is a sky simulation that is further based on an N -body dark matter simulation. The dark matter simulation is populated with galaxies from the Adding Density Determined GALaxies to Lightcone Simulations (ADDGALS) algorithm (DeRose et al. 2019).

We use the UFIG product that matches the footprint of the ‘gold’ sample in Section 2.2. The simulation is divided into fields of 0.53 deg^2 , with characteristic quantities like the image depth and seeing matching those of the DES-SV patches. SEXTRACTOR is applied to the simulated images with identical DES-SV settings. We select objects with $\text{magerr_auto} < 0.218 \text{ mag}$ in z (5σ significance), derive their observed magnitude distribution, and compare it to the truth magnitude distribution of all input truth objects (see illustration about the procedure in Fig. A1). The ratio between the two is well described by equation (A1). The derived m_{50} and w are tightly related to the depth of the image as shown in Fig. A2.

We also perform the analysis with the BALROG simulation (Suchyta et al. 2016), which inserts simulated objects into real DES-SV images. The results are similar.

To further verify the derived relations, we stack high-quality images from the DES Supernovae survey (with a total exposure time of $\sim 1000 \text{ s}$) to mimic main survey depth. The z -band depth of the stacks ranges from 21.5 to 22.5 mag, comparing to $> 24 \text{ mag}$ coadding all eligible exposures. We compare the object counts in this set of coadds and the full coadds to evaluate m_{50} and w (also shown in Fig. A2).

The m_{50} appears to be 0.1–0.4 mag deeper than the simulation relations. The effect is consistent with the mag_auto biases shown in Z16. In this test, we compare to the observed Kron magnitudes rather than the ‘truth’ magnitudes (which is not known) from the deeper stack. Z16 shows that the observed Kron magnitudes are fainter by 0.1–0.4 mag comparing to the ‘truth’ magnitudes at $< 24 \text{ mag}$.

Fig. A2 indicates that the amplitude of the complementary error function is lower than 1 in UFIG and BALROG. This is mostly caused by the same photometry measurement bias discussed above (another effect is the blending of truth objects, which causes incompleteness at a < 2 percent level). Objects are measured fainter by the Kron magnitude. Compared to the truth magnitude distribution, the observed magnitude distribution is systematically shifted to the fainter side (see this effect in Fig. A1). The result is that the observed magnitude distribution is always lower than the truth distribution, and the amplitude of the fitted completeness function is below 1. This shift and the resulting amplitudes of the completeness function are not of interest in this paper. We explicitly assume the amplitudes of the completeness function to be 1.

¹¹Magnitude with $\text{magerr_auto} = 0.108$. For a flux measurement at a significance level of 10σ , the corresponding magnitude uncertainty is $2.5/\ln 10/10 = 0.108$.

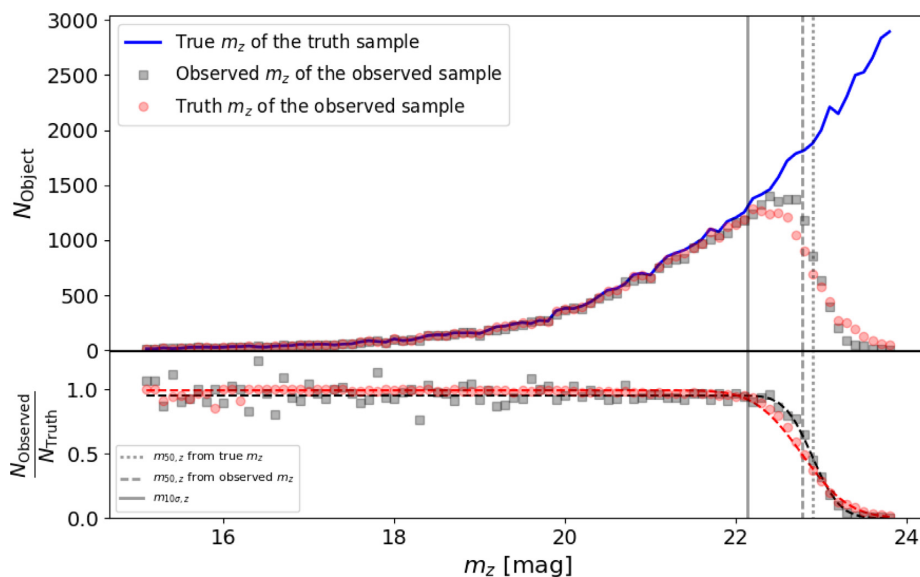


Figure A1. This figure demonstrates our procedure for evaluating completeness function with the UFIG simulation. We model the difference between the observed magnitude distribution (grey squares in the upper panel) of observed objects and the true magnitude distribution of all truth objects (solid blue line in the top panel). We model the ratio between the observed magnitude distribution and the truth magnitude distribution (grey squares in the lower panel) with a complementary error function (black dashed line). For comparison, we also show ratios between the truth magnitude distributions of the observed and the truth objects (red circles) and the complementary error function fitted model (red dashed line).

We notice hints that the completeness function in galaxy clusters are different from that of the fields, possibly because of blending and larger galaxy sizes. We test the effect with simulated objects (BALROG simulation, Suchyta et al. 2016) inserted into RedMaPPer clusters (Rykoff et al. 2016) selected in DES-SV data. We see evidence that the m_{50} inside galaxy clusters shift by ~ 0.1 mag comparing to fields of equivalent depth (Fig. A3). As the sample of simulated galaxies is small, we are unable to characterize the distribution of the shifts and hence do not attempt to correct m_{50} in this paper.

A3 Completeness limits of the RSLF analyses

We determine the magnitude limits of the RSLF analyses according to the completeness functions. We perform the analyses only with galaxies brighter than the following limit: $m_{\text{lim}} = m_{50} - 2\sqrt{2w}$. The cut ensures detection probability above 99.8 per cent $\times \lambda$ for the selected galaxies, according to our fitted completeness function model (equation A1). Note that the completeness limit is close to the 10σ total magnitude limit, which means galaxies above the completeness limit shall have total magnitude measured with significance level above or close to 10σ , and hence above surface brightness detection limit set at the detection (1.5σ in SEXTRACTOR

set-up), and therefore any surface brightness selection effects should be negligible.

If the cluster region completeness functions follow different relations as discussed above, the magnitude cut still ensures high detection probability (lower limit of 99 per cent $\times \lambda$ instead of 99.8 per cent $\times \lambda$).

For all of the $z < 0.4$ clusters, m_{lim} is more than 2 mag fainter than the characteristic magnitude measured in Hansen et al. (2009). This is also true for more than 2/3 of the clusters at $z > 0.4$. The cluster sample size drops steeply above redshift 0.7, and most of the complete clusters are located in the DES deep supernovae fields. As the galaxy samples are highly complete, we do not correct detection probability in this paper.

Because the g , r , i , z -band observations are performed independently, one may wonder if the image depth in the bluer bands is sufficient for computing colours. For example, the i -band observation of an object detected in z may be too shallow that it does not have valid i -band photometry measurement. We confirm that after applying the z -band magnitude limit cut ($\text{mag_auto_}z < m_{\text{lim}}$), 99.5 per cent and 99.6 per cent of the cluster region objects are detected in r and i , respectively. 98.3 per cent or 99.2 per cent of the objects have good r - or i -band photometry measurement (magerr_auto above 3σ , i.e. $\text{magerr_auto} < 2.5/\ln(10/3)$). We conclude that the DES multiband data are sufficiently deep for red-galaxy selection.

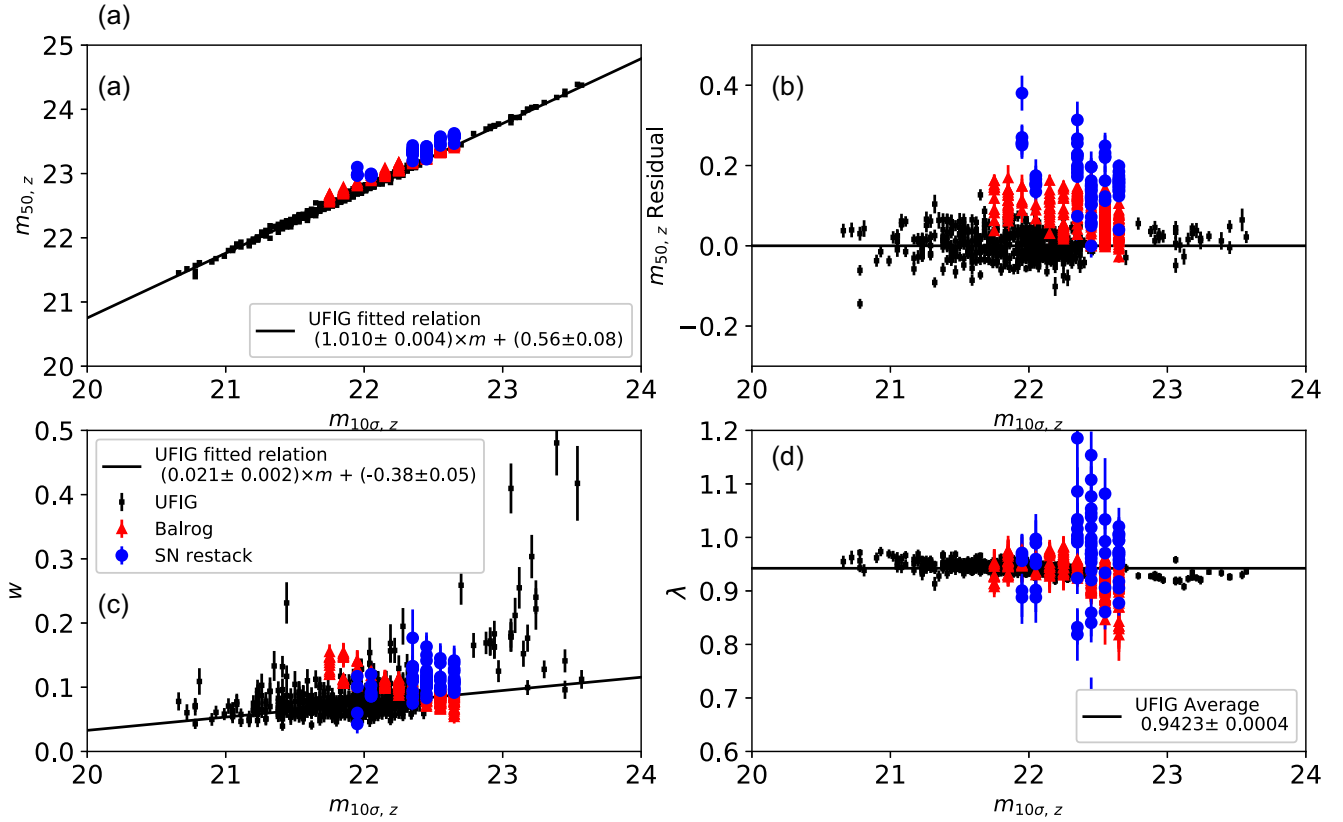


Figure A2. This figure shows the relations between completeness function parameters and the image depth, characterized by the 10σ limiting magnitude. Panel (a) shows the dependences of m_{50} , the 50 per cent completeness magnitude, on image depth from the UFIG (black points), BALROG (red triangles) simulations and the SN restack data (blue circles). Panel (b) shows the m_{50} residuals of the three data sets from the UFIG relation. The relation derived with the UFIG simulation generally agrees with the data from the BALROG simulation. The m_{50} values evaluated from re-stacking deep supernovae data appear to be 0.1–0.2 mag deeper, but the differences can be explained by the Kron magnitude bias shown in Z16. Panel (c) shows the dependences of w , the steepness of the detection drop-out rate, on image depth. We use the UFIG simulation relations for both m_{50} and w in this paper. We notice that the completeness function amplitudes from simulations appear to be lower than 1 as shown in panel (d), but it is mostly caused by the differences between observed and truth magnitudes (see a discussion in Section A2).

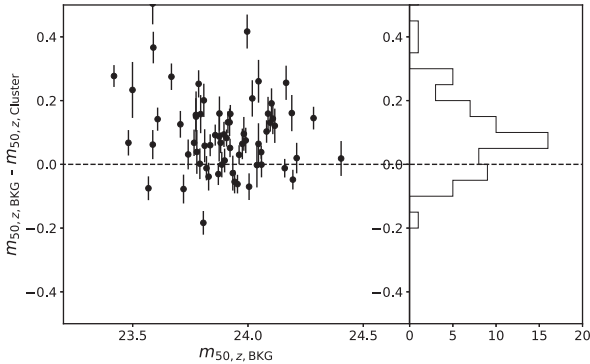


Figure A3. We evaluate the m_{50} parameters (50 per cent completeness magnitudes) for cluster and for field regions of the same depth with the BALROG simulation. The m_{50} of a cluster region is potentially shallower by ~ 0.1 mag compared to a same-depth field region potentially because of blending in the cluster region.

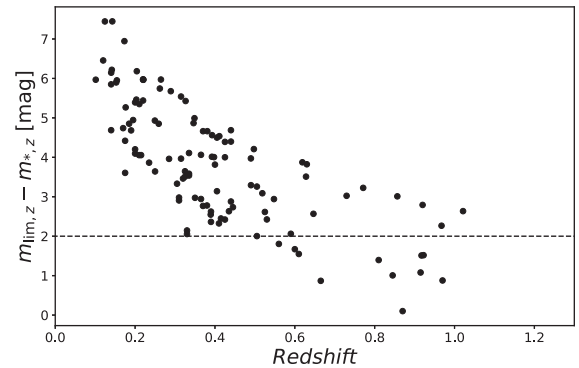


Figure A4. For each cluster, we derive a completeness limit, m_{lim} from the completeness function. At $z < 0.4$, all of the DES XCS-SV clusters are complete to $m_{z^*} + 2$ mag and beyond. This is also true for more than 2/3 of the clusters at $z > 0.4$. Incomplete clusters of m_{lim} below $m_{z^*} + 2$ mag are not included in this paper's analyses. The scatters of m_{lim} are caused by DES depth variations in different parts of the sky.

APPENDIX B: CLUSTER INFORMATION

Table B1. Information of the clusters used in this analysis.

Cluster designation	RA	Dec.	$\log(M_{200}/M_{\odot})$	Cluster redshift
XCSJ003248.5–431407.0	8.202084	–43.235279	14.02 ± 0.16	0.3923 ^a
XCSJ003321.0–433737.1	8.337500	–43.626972	14.08 ± 0.31	0.3809 ^a
XCSJ003346.3–431729.7	8.442917	–43.291584	14.23 ± 0.12	0.2199 ^a
XCSJ003407.6–432236.2	8.531667	–43.376720	13.89 ± 0.19	0.3928 ^a
XCSJ003428.0–431854.2	8.616667	–43.315056	14.37 ± 0.10	0.3977 ^a
XCSJ003429.6–434715.7	8.623333	–43.787693	13.47 ± 0.14	0.2042 ^a
XCSJ003518.1–433402.4	8.825417	–43.567333	14.00 ± 0.12	0.4400 ^a
XCSJ003545.5–431756.0	8.939584	–43.298889	13.48 ± 0.19	0.4109 ^a
XCSJ003548.1–432232.8	8.950417	–43.375778	14.25 ± 0.16	0.6280 ^a
XCSJ003627.6–432830.3	9.115000	–43.475082	13.94 ± 0.18	0.42
XCSJ004157.8–442026.5	10.490833	–44.340694	13.94 ± 0.21	0.36
XCSJ021433.4–042909.9	33.639168	–4.486084	14.77 ± 0.12	0.1401 ^a
XCSJ021441.2–043313.8	33.671665	–4.553833	14.70 ± 0.11	0.1416 ^a
XCSJ021529.0–044052.8	33.870834	–4.681334	14.31 ± 0.16	0.34
XCSJ021612.5–041426.2	34.052082	–4.240611	14.32 ± 0.15	0.1543 ^a
XCSJ021653.2–041723.7	34.221668	–4.289917	13.36 ± 0.17	0.1527 ^a
XCSJ021734.7–051327.6	34.394585	–5.224333	14.08 ± 0.23	0.6467 ^a
XCSJ021741.6–045148.0	34.423332	–4.863333	13.74 ± 0.26	0.5187 ^a
XCSJ021755.3–052708.0	34.480415	–5.452222	13.74 ± 0.18	0.2495 ^a
XCSJ021803.4–055526.5	34.514168	–5.924028	14.11 ± 0.26	0.3893 ^a
XCSJ021843.7–053257.6	34.682083	–5.549333	13.73 ± 0.21	0.40
XCSJ021946.1–050748.2	34.942081	–5.130055	14.44 ± 0.37	0.4902 ^a
XCSJ022024.7–050232.0	35.102917	–5.042222	14.39 ± 0.16	0.12
XCSJ022034.4–054348.7	35.143333	–5.730195	14.21 ± 0.26	0.20
XCSJ022042.7–052550.0	35.177917	–5.430555	13.90 ± 0.21	0.5477 ^a
XCSJ022156.8–054521.9	35.486668	–5.756083	14.08 ± 0.11	0.2591 ^a
XCSJ022204.5–043239.4	35.518749	–4.544278	14.17 ± 0.29	0.3150 ^a
XCSJ022234.0–045759.8	35.641666	–4.966611	13.77 ± 0.24	0.92
XCSJ022258.7–040637.9	35.744583	–4.110528	14.01 ± 0.33	0.2893 ^a
XCSJ022307.9–041257.2	35.782917	–4.215889	13.74 ± 0.31	0.6300 ^a
XCSJ022318.6–052708.2	35.827499	–5.452278	13.61 ± 0.14	0.2106 ^a
XCSJ022342.3–050200.9	35.926250	–5.033583	13.72 ± 0.18	0.8568 ^a
XCSJ022347.6–025127.1	35.948334	–2.857528	14.10 ± 0.18	0.17
XCSJ022357.5–043520.7	35.989582	–4.589083	14.16 ± 0.32	0.4974 ^a
XCSJ022401.9–050528.4	36.007915	–5.091222	13.99 ± 0.15	0.3265 ^a
XCSJ022405.8–035505.5	36.024166	–3.918195	14.32 ± 0.36	0.44
XCSJ022433.9–041432.7	36.141251	–4.242417	13.91 ± 0.13	0.2619 ^a
XCSJ022457.9–034849.4	36.241249	–3.813722	14.35 ± 0.15	0.6189 ^a
XCSJ022509.7–040137.9	36.290417	–4.027194	13.89 ± 0.17	0.1732 ^a
XCSJ022512.2–062305.1	36.300835	–6.384750	14.56 ± 0.15	0.2031 ^a
XCSJ022524.8–044043.4	36.353333	–4.678722	14.26 ± 0.15	0.2647 ^a
XCSJ022530.8–041421.1	36.378334	–4.239194	14.20 ± 0.12	0.1429 ^a
XCSJ022532.0–035509.5	36.383335	–3.919306	14.30 ± 0.25	0.7712 ^a
XCSJ022808.6–053543.6	37.035831	–5.595445	13.71 ± 0.13	0.21
XCSJ023037.2–045929.5	37.654999	–4.991528	14.10 ± 0.21	0.31
XCSJ023052.4–045123.5	37.718334	–4.856528	14.01 ± 0.15	0.31
XCSJ023142.2–045253.1	37.925835	–4.881417	14.66 ± 0.11	0.20
XCSJ033150.1–273946.1	52.958752	–27.662806	13.66 ± 0.18	1.0213 ^a
XCSJ034106.0–284132.2	55.275002	–28.692278	14.60 ± 0.39	0.51
XCSJ041328.7–585844.3	63.369583	–58.978973	13.64 ± 0.14	0.14
XCSJ041644.8–552506.6	64.186668	–55.418499	14.24 ± 0.20	0.41
XCSJ042017.5–503153.9	65.072914	–50.531639	14.17 ± 0.11	0.45
XCSJ043750.2–541940.8	69.459167	–54.327999	13.83 ± 0.13	0.21
XCSJ043818.3–541916.5	69.576248	–54.321251	14.94 ± 0.12	0.42
XCSJ065744.2–560817.0	104.434166	–56.138054	14.14 ± 0.14	0.32
XCSJ065900.5–560927.5	104.752083	–56.157639	14.08 ± 0.25	0.33
XCSJ095823.4+024850.9	149.597504	2.814139	14.56 ± 0.15	0.41
XCSJ095901.2+024740.4	149.755005	2.794556	13.90 ± 0.18	0.4900 ^a
XCSJ095902.7+025544.9	149.761246	2.929139	14.44 ± 0.13	0.3487 ^a
XCSJ095924.7+014614.1	149.852921	1.770583	13.96 ± 0.15	0.1243 ^a
XCSJ095932.1+022634.6	149.883743	2.442945	14.24 ± 0.25	0.42

Table B1 – *continued*

Cluster designation	RA	Dec.	$\log(M_{200}/M_{\odot})$	Cluster redshift
XCSJ095940.7+023110.8	149.919586	2.519667	14.67 ± 0.15	0.7297 ^a
XCSJ095951.2+014045.8	149.963333	1.679389	14.11 ± 0.15	0.3702 ^a
XCSJ100023.1+022358.0	150.096252	2.399444	13.86 ± 0.13	0.22
XCSJ100027.1+022131.7	150.112915	2.358806	14.01 ± 0.16	0.2207 ^a
XCSJ100043.0+014559.2	150.179169	1.766444	14.30 ± 0.18	0.3464 ^a
XCSJ100047.3+013927.8	150.197083	1.657722	14.39 ± 0.11	0.2200 ^a
XCSJ224857.4–443013.6	342.239166	–44.503777	15.08 ± 0.14	0.36
XCSJ232447.6–552443.3	351.198334	–55.412029	13.91 ± 0.17	0.30
XCSJ232632.7–563054.5	351.636261	–56.515141	13.73 ± 0.14	0.17
XCSJ232633.3–550116.3	351.638763	–55.021194	14.41 ± 0.17	0.43
XCSJ232645.9–534839.3	351.691254	–53.810917	13.55 ± 0.13	0.20
XCSJ232804.7–563004.5	352.019592	–56.501251	14.15 ± 0.18	0.19
XCSJ232940.9–544715.3	352.420410	–54.787582	13.71 ± 0.19	0.14
XCSJ232956.6–560808.0	352.485840	–56.135555	14.32 ± 0.14	0.44
XCSJ233000.5–543706.3	352.502075	–54.618416	14.34 ± 0.12	0.1763 ^a
XCSJ233037.2–554340.2	352.654999	–55.727833	14.23 ± 0.28	0.33
XCSJ233132.2–531104.3	352.884155	–53.184528	13.79 ± 0.17	0.41
XCSJ233133.8–562804.6	352.890839	–56.467945	14.01 ± 0.29	0.18
XCSJ233204.9–551242.9	353.020416	–55.211918	13.73 ± 0.16	0.34
XCSJ233216.0–544205.5	353.066681	–54.701527	14.37 ± 0.19	0.32
XCSJ233225.7–560237.5	353.107086	–56.043751	14.14 ± 0.18	0.28
XCSJ233403.8–554903.9	353.515839	–55.817749	14.35 ± 0.35	0.34
XCSJ233706.9–541909.8	354.278748	–54.319389	13.81 ± 0.31	0.53
XCSJ233835.2–543729.5	354.646667	–54.624863	14.67 ± 0.28	0.38
XCSJ233955.1–561519.6	354.979584	–56.255444	14.06 ± 0.39	0.37
XCSJ234054.4–554256.6	355.226654	–55.715721	13.43 ± 0.15	0.17
XCSJ234142.9–555748.9	355.428741	–55.963585	14.35 ± 0.16	0.20
XCSJ234231.5–562105.9	355.631256	–56.351639	14.37 ± 0.14	0.35
XCSJ234311.1–555249.8	355.796265	–55.880501	13.84 ± 0.20	0.23
XCSJ234600.9–561104.8	356.503754	–56.184666	13.52 ± 0.14	0.1014 ^a
XCSJ234806.2–560121.1	357.025848	–56.022530	14.79 ± 0.32	0.39
XCSJ235810.2–552550.1	359.542511	–55.430584	14.57 ± 0.16	0.25

^a Archive spectroscopic redshift.¹ Fermi National Accelerator Laboratory, PO Box 500, Batavia, IL 60510, USA² Department of Astronomy, University of Michigan, Ann Arbor, MI 48109, USA³ Department of Physics, University of Michigan, Ann Arbor, MI 48109, USA⁴ Department of Physics and Astronomy, Pevensey Building, University of Sussex, Brighton BN1 9QH, UK⁵ Kavli Institute for Particle Astrophysics & Cosmology, PO Box 2450, Stanford University, Stanford, CA 94305, USA⁶ SLAC National Accelerator Laboratory, Menlo Park, CA 94025, USA⁷ Faculty of Physics, Ludwig-Maximilians-Universität, Scheinerstr 1, D-81679 Munich, Germany⁸ Excellence Cluster Universe, Boltzmannstr 2, D-85748 Garching, Germany⁹ Taejeon Christian International School, Yuseong, Daejeon 34035, South Korea¹⁰ Institute of Cosmology & Gravitation, University of Portsmouth, Portsmouth PO1 3FX, UK¹¹ Jodrell Bank Center for Astrophysics, School of Physics and Astronomy, University of Manchester, Oxford Road, Manchester M13 9PL, UK¹² Astrophysics Research Institute, Liverpool John Moores University, IC2, Liverpool Science Park, 146 Brownlow Hill, Liverpool L3 5RF, UK¹³ School of Physics and Astronomy, University of Nottingham, Nottingham NG7 2RD, UK¹⁴ Astrophysics and Cosmology Research Unit, School of Mathematics, Statistics and Computer Science, University of KwaZuluNatal, Westville Campus, Durban 4000, South Africa¹⁵ Fakultät für Physik, Universitäts-Sternwarte, Ludwig-Maximilians Universität München, Scheinerstr 1, D-81679 München, Germany¹⁶ Jodrell Bank Centre for Astrophysics, School of Physics and Astronomy, The University of Manchester, Manchester M13 9PL, UK¹⁷ Institute for Astronomy, University of Edinburgh, Edinburgh EH9 3HJ, UK¹⁸ Institute for Astronomy, University of Edinburgh, Royal Observatory, Blackford Hill, Edinburgh EH9 3HJ, UK¹⁹ George P. and Cynthia Woods Mitchell Institute for Fundamental Physics and Astronomy, and Department of Physics and Astronomy, Texas A&M University, College Station, TX 77843, USA²⁰ Department of Physics and Astronomy, Uppsala University, Box 516, SE-751 20 Uppsala, Sweden²¹ Physics Department, Lancaster University, Lancaster LA1 4YB, UK²² Instituto de Astrofísica e Ciências do Espaço, Universidade do Porto, CAUP, Rua das Estrelas, P-4150-762 Porto, Portugal²³ Departamento de Física e Astronomia, Faculdade de Ciências, Universidade do Porto, Rua do Campo Alegre 687, P-4169-007 Porto, Portugal²⁴ Department of Physics, Stanford University, 382 Via Pueblo Mall, Stanford, CA 94305, USA²⁵ Cerro Tololo Inter-American Observatory, National Optical Astronomy Observatory, Casilla 603, La Serena, Chile²⁶ Department of Physics & Astronomy, University College London, Gower Street, London WC1E 6BT, UK²⁷ Department of Physics and Electronics, Rhodes University, PO Box 94, Grahamstown 6140, South Africa²⁸ CNRS, UMR 7095, Institut d'Astrophysique de Paris, F-75014 Paris, France²⁹ Institut d'Astrophysique de Paris, Sorbonne Universités, UPMC Univ Paris 06, UMR 7095, F-75014 Paris, France

- ³⁰Laboratório Interinstitucional de e-Astronomia - LIneA, Rua Gal. José Cristino 77, Rio de Janeiro, RJ 20921-400, Brazil
- ³¹Observatório Nacional, Rua Gal. José Cristino 77, Rio de Janeiro, RJ 20921-400, Brazil
- ³²Department of Astronomy, University of Illinois, 1002 W. Green Street, Urbana, IL 61801, USA
- ³³National Center for Supercomputing Applications, 1205 West Clark St., Urbana, IL 61801, USA
- ³⁴Institut de Física d'Altes Energies (IFAE), The Barcelona Institute of Science and Technology, Campus UAB, E-08193 Bellaterra (Barcelona), Spain
- ³⁵Institute of Space Sciences, IEEC-CSIC, Campus UAB, Carrer de Can Magrans, s/n, E-08193 Barcelona, Spain
- ³⁶Department of Physics and Astronomy, University of Pennsylvania, Philadelphia, PA 19104, USA
- ³⁷Department of Physics, California Institute of Technology, Pasadena, CA 91125, USA
- ³⁸Jet Propulsion Laboratory, California Institute of Technology, 4800 Oak Grove Dr., Pasadena, CA 91109, USA
- ³⁹Instituto de Física Teórica UAM/CSIC, Universidad Autónoma de Madrid, E-28049 Madrid, Spain
- ⁴⁰Center for Cosmology and Astro-Particle Physics, The Ohio State University, Columbus, OH 43210, USA

- ⁴¹Department of Physics, The Ohio State University, Columbus, OH 43210, USA
- ⁴²Astronomy Department, University of Washington, Box 351580, Seattle, WA 98195, USA
- ⁴³Santa Cruz Institute for Particle Physics, Santa Cruz, CA 95064, USA
- ⁴⁴Australian Astronomical Observatory, North Ryde, NSW 2113, Australia
- ⁴⁵Departamento de Física Matemática, Instituto de Física, Universidade de São Paulo, CP 66318, São Paulo, SP 05314-970, Brazil
- ⁴⁶Department of Astrophysical Sciences, Princeton University, Peyton Hall, Princeton, NJ 08544, USA
- ⁴⁷Institució Catalana de Recerca i Estudis Avançats, E-08010 Barcelona, Spain
- ⁴⁸Centro de Investigaciones Energéticas, Medioambientales y Tecnológicas (CIEMAT), E-28040 Madrid, Spain
- ⁴⁹School of Physics and Astronomy, University of Southampton, Southampton SO17 1BJ, UK
- ⁵⁰Instituto de Física Gleb Wataghin, Universidade Estadual de Campinas, 13083-859 Campinas, SP, Brazil
- ⁵¹Computer Science and Mathematics Division, Oak Ridge National Laboratory, Oak Ridge, TN 37831, USA

This paper has been typeset from a \LaTeX file prepared by the author.